

Global Impact of COVID-19 Restrictions on the Surface Concentrations of Nitrogen Dioxide and Ozone

Christoph A. Keller^{1,2}, Mat. J. Evans^{3,4}, K. Emma Knowland^{1,2}, Christa A. Hasenkopf⁵, Sruti Modekurty⁵, Robert A. Lucchesi^{1,6}, Tomohiro Oda^{1,2}, Bruno B. Franca⁷, Felipe C. Mandarino⁷, M. Valeria Díaz Suárez⁸, Robert G. Ryan⁹, Luke H. Fakes^{3,4}, Steven Pawson¹

¹NASA Global Modeling and Assimilation Office, Goddard Space Flight Center, Greenbelt, MD, USA

²Universities Space Research Association, Columbia, MD, USA

³Wolfson Atmospheric Chemistry Laboratories, Department of Chemistry, University of York, York, YO10 5DD, UK

⁴National Centre for Atmospheric Science, University of York, York, YO10 5DD, UK

⁵OpenAQ, Washington, DC, USA

⁶Science Systems and Applications, Inc., Lanham, MD, USA

⁷Municipal Government of Rio de Janeiro, Rio de Janeiro, Brazil

⁸Secretaria de Ambiente, Quito, Ecuador

⁹School of Earth Sciences, The University of Melbourne, Australia

Correspondence to: Christoph A. Keller (christoph.a.keller@nasa.gov)

Abstract. Social-distancing to combat the COVID-19 pandemic has led to widespread reductions in air pollutant emissions. Quantifying these changes requires a business-as-usual counterfactual that accounts for the synoptic and seasonal variability of air pollutants. We use a machine learning algorithm driven by information from the NASA GEOS-CF model to assess changes in nitrogen dioxide (NO₂) and ozone (O₃) at 5,756 observation sites in 46 countries from January through June 2020. Reductions in NO₂ coincide with timing and intensity of COVID-19 restrictions, ranging from 60% in severely affected cities (e.g., Wuhan, Milan) to little change (e.g., Rio de Janeiro, Taipei). On average, NO₂ concentrations were 18 (13-23)% lower than business as usual from February 2020 onward. China experienced the earliest and steepest decline, but concentrations since April have mostly recovered and remained within 5% to the business-as-usual estimate. NO₂ reductions in Europe and the US have been more gradual with a halting recovery starting in late March. We estimate that the global NO_x (NO+NO₂) emission reduction during the first 6 months of 2020 amounted to 3.1 (2.6-3.6) TgN, equivalent to 5.5 (4.7-6.4)% of the annual anthropogenic total. The response of surface O₃ is complicated by competing influences of non-linear atmospheric chemistry. While surface O₃ increased by up to 50% in some locations, we find the overall net impact on daily average O₃ between February - June 2020 to be small. However, our analysis indicates a flattening of the O₃ diurnal cycle with an increase in night time ozone due to reduced titration and a decrease in daytime ozone, reflecting a reduction in photochemical production.

The O₃ response is dependent on season, time scale, and environment, with declines in surface O₃ forecasted if NO_x emission reductions continue.

1 Introduction

40 The stay-at-home orders imposed in many countries during the Northern Hemisphere spring of 2020 to
slow the spread of the severe acute respiratory syndrome coronavirus 2 (SARS-CoV-2, hereafter
COVID-19), led to a sharp decline in human activities across the globe (Le Quéré et al., 2020). The
associated decrease in industrial production, energy consumption, and transportation resulted in a
reduction in the emissions of air pollutants, notably nitrogen oxides (NO_x=NO+NO₂) (Liu et al., 2020a;
Dantas et al., 2020; Petetin et al., 2020; Tobias et al., 2020; Le et al., 2020). NO_x has a short
45 atmospheric lifetime and are predominantly emitted during the combustion of fossil fuel for industry,
transport and domestic activities (Streets et al., 2013, Duncan et al., 2016). Atmospheric concentrations
of nitrogen dioxide (NO₂) thus readily respond to local changes in NO_x emissions (Lamsal et al., 2011).
While this may provide both air quality and climate benefits, a quantitative assessment of the magnitude
of these impacts is complicated by the natural variability of air pollution due to variations in synoptic
50 conditions (weather), seasonal effects, and long-term emission trends as well as the non-linear responses
between emissions and concentrations. Thus, simply comparing the concentration of pollutants during
the COVID-19 period to those immediately before or to the same period in previous years is not
sufficient to indicate causality. An emerging approach to address this problem is to develop machine-
learning based ‘weather-normalization’ algorithms to establish the relationship between local
55 meteorology and air pollutant surface concentrations (Grange et al., 2018; Grange and Carslaw, 2019;
Petetin et al., 2020). By removing the meteorological influence, these studies have tried to better
quantify emission changes as a result of a perturbation.

Here we adapt this weather-normalization approach to not only include meteorological information but
60 also compositional information in the form of the concentrations and emissions of chemical
constituents. Using a collection of surface observations of NO₂ and ozone (O₃) from across the world
from 2018 to present (Section 2.1), we develop a ‘bias-correction’ methodology for the NASA global
atmospheric composition model GEOS-CF (Section 2.2) which corrects the model output at each
observational site based on the observations for 2018 and 2019 (Section 2.3). These biases reflect errors
65 in emission estimates, sub-gridscale local influences (representational error), or meteorology and
chemistry. Since the GEOS-CF model makes no adjustments to the anthropogenic emissions in 2020,
and no 2020 observations are included in the training of the bias corrector, the bias-corrected model
(hereafter BCM) predictions for 2020 represent a business-as-usual scenario at each observation site
that can be compared against the actual observations. This allows the impact of COVID-19 containment
70 measures on air quality to be explored, taking into account meteorology and the long-range transport of
pollutants. We first apply this to the concentration of NO₂ (Section 3.1), and then O₃ (Section 3.2) and
explore the differences between the counterfactual prediction and the observed concentrations. In
Section 3.3 we explore how the observed changes in the NO₂ concentrations relate to emission of NO_x,

75 and in Section 3.4 we speculate what the COVID-19 restrictions might mean for the second half of 2020.

2 Methods

2.1 Observations

80 Our analysis builds on the recent development of unprecedented public access to air pollution model output and air quality observations in near real-time. We compile an air quality dataset of hourly surface observations for a total of 5,756 sites (4,778 for NO₂ and 4,463 for O₃) in 46 countries for the time period January 1, 2018 to July 1, 2020, as summarized in Fig. 1 and Table 1. More detailed maps of the spatial distribution of observation sites over China, Europe, and North America are given in Fig A1-3. The vast majority of the observations were obtained from the OpenAQ platform and the air quality data portal of the European Environment Agency (EEA). Both platforms provide harmonized air quality
85 observations in near real-time, greatly facilitating the analysis of otherwise disparate data sources. For the EEA observations, we use the validated data (E1a) for years 2018-2019 and revert to the real-time data (E2a) for 2020. For Japan, we obtained hourly surface observations for a total of 225 sites in Hokkaido, Osaka, and Tokyo from the Atmospheric Environmental Regional Observation System (AEROS) (MOE, 2020). To improve data coverage in under-sampled regions, we further included
90 observations from the cities of Rio de Janeiro (Brazil), Quito (Ecuador), and Melbourne (Australia). All cities offer continuous, hourly observations of NO₂ and O₃ over the full analysis period, thus offering an excellent snapshot of air quality at these locations. We include all sites with at least 365 days of observations between Jan 1, 2018 and December 31, 2019, and an overall data coverage of 75% or more since the first day of availability. Only days with at least 12 hours of valid data are included in the
95 analysis. The final NO₂ and O₃ dataset comprise 8.9×10^7 and 8.2×10^7 hourly observations, respectively.

Observation sites

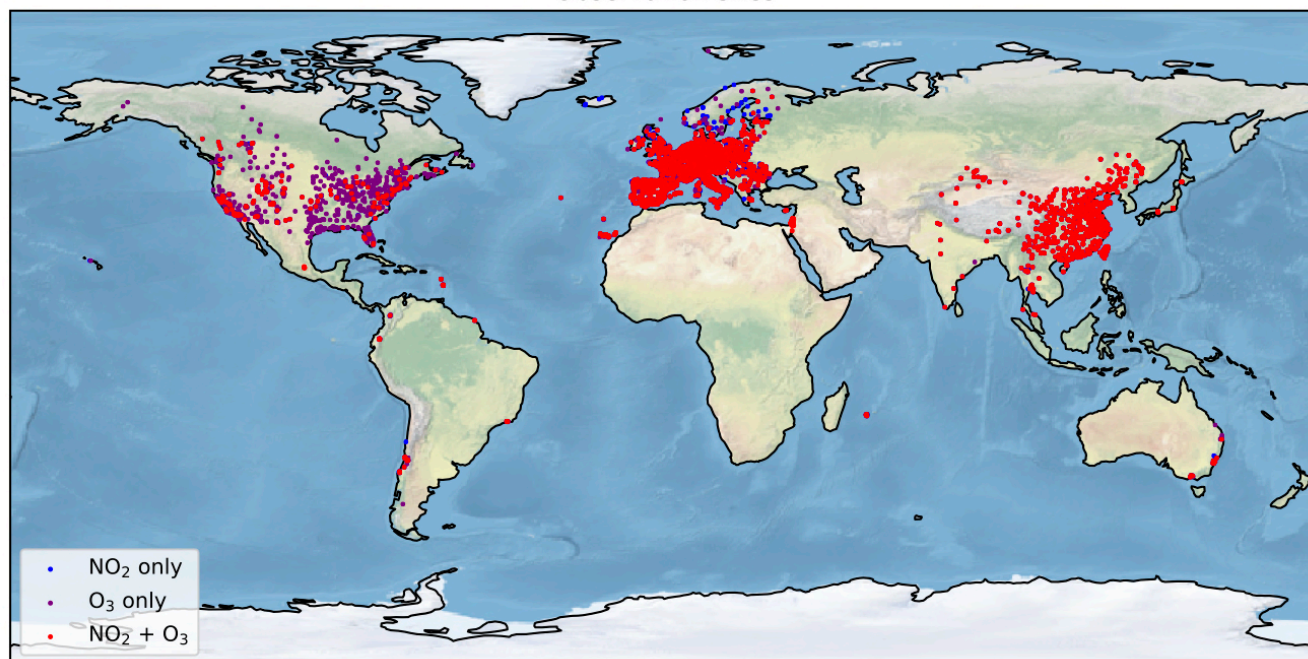


Figure 1: Location of the 5,756 observation sites included in the analysis. Red points indicate sites with both NO₂ and O₃ observations (3,485 in total), purple points show locations with O₃ observations only (978 sites) and blue points show locations with NO₂ observations only (1,293 sites). See Appendix for detailed maps for North America, Europe, and China.

100 **Table 1:** Observational data sources used in the analysis. Time period covers Jan 1, 2018 - July 1, 2020.

Name	Countries	Sites	Source
OpenAQ	Australia, China, India, Hong Kong, Taiwan, Thailand, Canada, Chile, Colombia, United States	2410	https://openaq.org/
EEA	Austria, Belgium, Bosnia and Herzegovina, Bulgaria, Croatia, Cyprus, Czech Republic, Denmark, Estonia, Finland, France, Germany, Greece, Hungary, Iceland, Ireland, Italy, Latvia, Lithuania, Luxembourg, Macedonia, Malta, Netherlands, Norway, Poland, Portugal, Romania, Serbia, Slovakia, Slovenia, Spain, Sweden, Switzerland, United Kingdom,	3101	https://discomap.eea.europa.eu/map/fme/AirQualityExport.htm
AEROS	Japan	225	http://soramame.taiki.go.jp/Index.php
EPA Victoria	Australia (Melbourne)	4	http://sciwebsvc.epa.vic.gov.au/aqapi/Help
Secretaria de Ambiente, Quito	Ecuador (Quito)	8	http://www.quitoambiente.gob.ec/ambiente/index.php/datos-horarios-historicos

Municipal Government of Rio de Janeiro	Brazil (Rio de Janeiro)	8	http://www.data.rio/datasets/dados-hor%C3%A1rios-do-monitoramento-da-qualidade-do-ar-monitorar
--	-------------------------	---	---

2.2 Model

105 Meteorological and atmospheric chemistry information at each of the air quality observation sites is obtained from the NASA Goddard Earth Observing System Composition Forecast (GEOS-CF) model (Keller et al., 2020). GEOS-CF integrates the GEOS-Chem atmospheric chemistry model (v12-01) into the GEOS Earth System Model (Long et al., 2015; Hu et al., 2018) and provides global hourly analyses of atmospheric composition at 25x25 km² spatial resolution, available in near real-time at https://gmao.gsfc.nasa.gov/weather_prediction/GEOS-CF/data_access/ (Knowland et al., 2020). Anthropogenic emissions are prescribed using monthly Hemispheric Transport of Air Pollution (HTAP) bottom-up emissions (Janssens-Maenhout et al., 2015), with imposed weekly and diurnal scale factors as described in Keller et al. (2020). The same anthropogenic base emissions are used for years 2018-2020. Therefore, GEOS-CF does not account for any anthropogenic emission changes since 2018, notably any anthropogenic emission reductions related to COVID-19 restrictions. However, it does capture the variability in natural emissions such as wildfires (based on the Quick Fire Emissions Dataset, QFED) (Darmenov and Da Silva, 2015), or lightning and biogenic emissions (Keller et al., 2014). While the meteorology and stratospheric ozone in GEOS-CF are fully constrained by pre-computed analysis fields produced by other GEOS systems (Lucchesi, 2015; Wargan et al., 2015), no trace-gas observations are directly assimilated into the current version of GEOS-CF. It thus provides a “business as usual” estimate of NO₂ and O₃ that can be used as a baseline for input into the meteorological normalization process.

120 2.3 Machine learning bias correction

2.3.1 Overall strategy

125 We use the XGBoost machine learning algorithm (<https://xgboost.readthedocs.io/en/latest/#>) (Chen and Guestrin, 2016; Frery et al., 2017) to develop a machine learning model to predict the time-varying bias at each observation site at an hourly scale. XGBoost uses the Gradient Boosting framework to build an ensemble of decision trees, trained iteratively on the residual errors to stage-wise improve the model predictions (Friedman, 2001). Based on the 2018-2019 observation-model differences, the machine learning model is trained to predict the systematic (recurring) model bias between hourly observations and the co-located model predictions. These biases can be due to errors in the model, such as emission estimates, sub-gridscale local influences (representational error), or meteorology and chemistry. Since 130 model biases are often site-specific, we train a separate machine learning model for each site. The design of the XGBoost framework is determined by a set of hyperparameters, such as the learning rate, maximum tree depth, or minimum loss reduction. While a full hyperparameter optimization across all sites - e.g., by using a grid search approach – would be computationally prohibitive, we conducted hyperparameter sensitivity tests at few selected sites and found that the XGBoost performance only

135 improved marginally at these sites when using other hyperparameter than the model defaults (less than
5% improvement). In addition, we found that the sites respond differently to the same change in
hyperparameter setup, suggesting that there is no uniform hyperparameter design that is optimal across
all sites. Based on this, we chose to use the default XGBoost model parameters at all locations, with a
learning rate of 0.3, minimum loss reduction of 0, maximum tree depth of 6, and L1 and L2

140 regularization terms of 0 and 1, respectively.

For each location, we split the 2-year training dataset into 8 quarterly segments (Jan-Mar, Apr-Jun, etc.)
and train the model 8 times, each time omitting one of the segments (8-fold cross validation). The
omitted segment is used as test data to validate the general performance of the machine learning model
and to provide an uncertainty estimate, as further discussed below. This approach aims to reduce the
145 auto-correlation signal that can lead to overly optimistic machine-learning results (Kleinert et al., 2020)
while still including data from all four seasons in the testing. Once trained, the final model prediction at
each location consists of the average prediction of the eight models.

The observations used in this analysis are not always quality-controlled, which can cause issues if
erroneous observations are included in the training, such as unrealistically high O₃ concentrations of
150 several thousand ppbv. As an ad-hoc solution to this problem, we remove all observations below or
above 2 standard deviations from the annual mean from the analysis. Sensitivity tests using more
stringent thresholds of 3 or even 4 standard deviations resulted in no significant change in our results.

2.3.2 Evaluation of model predictors

155 The input variables fed into the XGBoost algorithm are provided in Table A1. The input features
encompass 9 meteorological parameters (as simulated by the GEOS-CF model: surface north- and
eastward wind components, surface temperature and skin temperature, surface relative humidity, total
cloud coverage, total precipitation, surface pressure, and planetary boundary layer height), modelled
surface concentrations of 51 chemical species (O₃, NO_x, carbon monoxide, VOCs, and aerosols), and 21
160 modelled emissions at the given location. In addition, we provide as input features the hour-of-day, day
of week, and month of the year; these allow the machine learning model to identify systematic
observation-model mismatches related to the diurnal, weekly and seasonal cycle of the pollutants. In
addition, for sites with observations available for the full two years, we provide the calendar days since
Jan 1, 2018 as an additional input feature to also correct for inter-annual trends in air pollution, e.g., due
165 to a steady decrease in emissions not captured by the model. This follows a similar technique to Ivatt
and Evans (2020) and Petetin et al. (2020).

Gradient boosted tree models consist of a tree-like decision structure, which can be analysed to
understand how the model uses the input features to make a prediction. Particularly useful in this
context is the SHapely Additive exPlanations (SHAP) approach, which is based on game-theoretic
170 Shapely values and represents a measure of each feature's responsibility for a change in the model
prediction (Lundberg et al., 2018). SHAP values are computed separately for each individual model
prediction, offering detailed insight into the importance of each input feature to this prediction while
also considering the role of feature interactions (Lundberg et al., 2020). In addition, combining the local
SHAP values offers a representation of the global structure of the machine learning model.

175 Figure A4 shows the distribution of the SHAP values for all NO₂ predictors separated by polluted sites (left panel) and non-polluted sites (right panel), with polluted sites defined as locations with an annual average NO₂ concentration of more than 15 ppbv. Generally, the model-predicted (unbiased) NO₂ concentration is the most important predictor for the model bias, followed by the hour of the day, the day since Jan 1st 2018 ('Trendday'), and a suite of meteorological variables including wind speed
180 (u10m, v10m), planetary boundary height (zpb1), and specific humidity (q10m). All of these factors are expected to highly impact NO₂ concentrations and it is thus not surprising that the model biases are most sensitive to them. While there is considerable spread in the feature importance across the individual sites, there is little overall difference in the feature ranking between polluted vs. non-polluted sites.

185 Figure A5 shows the SHAP value distribution for all O₃ predictors, again separated into polluted and non-polluted sites (using the same definition as for the NO₂ sites). Unlike for NO₂, the bias-correction models for polluted sites exhibit different feature sensitivities than the non-polluted sites. At polluted locations, the availability of reactive nitrogen (NO₂, NO_y, PAN) is the dominant factor for explaining the model O₃ bias, reflecting the tight chemical coupling between NO_x and O₃ (Seinfeld and Pandis,
190 2016). This is followed by the month of the year, total precipitation (tprec) and O₃ concentration, again variables expected to be correlated to O₃. At non-polluted sites, the uncorrected O₃ concentration is on average the most relevant input feature for the bias correctors, followed by the month of the year and the odd oxygen concentration (ox). The non-polluted sites are generally more sensitive to wind speed, reflecting the fact that O₃ production and loss at these locations is less dominated by local processes
195 compared to the polluted sites.

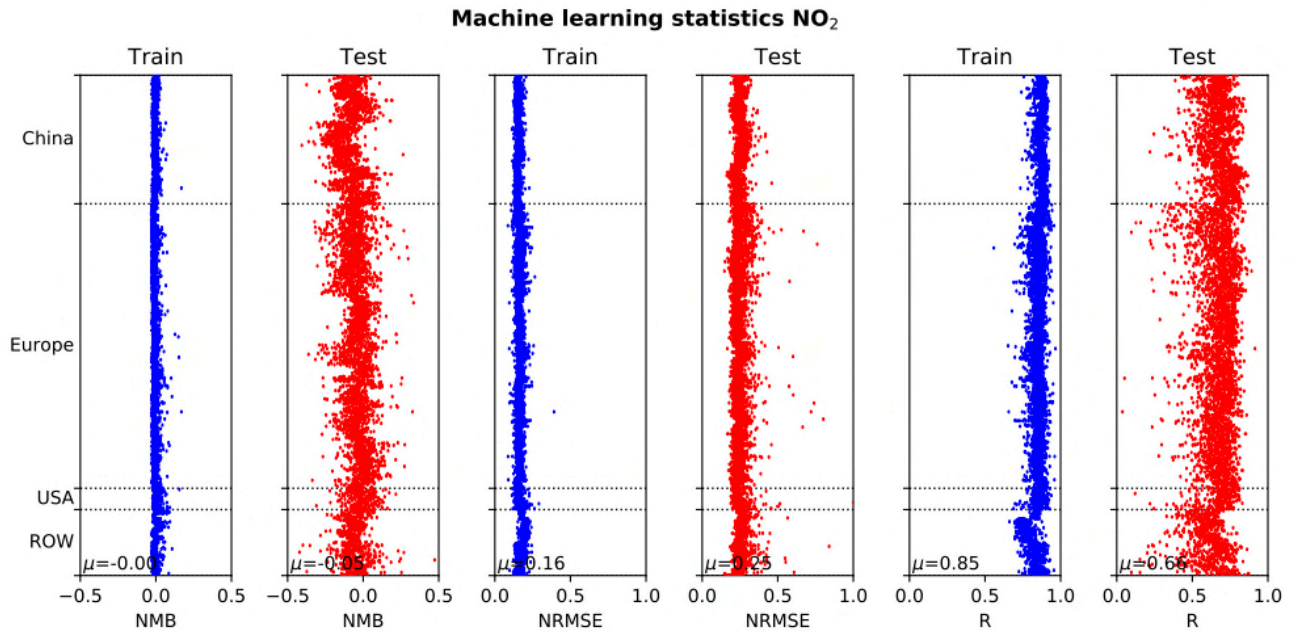
2.3.3 Machine learning model skill scores

Figures 2 and 3 summarize the machine learning model statistics for NO₂ and O₃, respectively. The normalized mean bias (NMB), normalized root mean square error (NRMSE), and Pearson correlation
200 coefficient (R) at each site are shown for both the training (blue) and the test (red) dataset. We define NMB as mean bias normalized by average concentration at the given site, and the NRMSE as the root mean square error normalized by the range of the 95-percentile concentration and 5-percentile concentration. Rather than using the mean as the denominator for the NRMSE, we choose the percentile window as a better reference point for the concentration variability at a given site. Using the mean as
205 the denominator for the NRMSE would lead to very similar qualitative results.

For both NO₂ and O₃, the bias-corrected model predictions show no bias when evaluated against the training data, NRMSE's of less than 0.3, and correlation coefficients between 0.6-1.0 (NO₂) and 0.75-1.0 (O₃). Compared to the training data, the skill scores on the test data show a higher variability, with an average NMB of -0.047 for NO₂ and -0.034 for O₃, a NRMSE of 0.25 (NO₂) and 0.18 (O₃), and a
210 correlation of 0.64 (NO₂) and 0.84 (O₃). We find no significant difference in skill scores between background vs. polluted sites or different countries.

A number of factors likely contribute to the poorer statistical results at some of the sites. Importantly, some sites might be prone to overfitting if the training data includes events that are not easily generalizable, such as unusual emission activity (e.g., biomass burning, fireworks, closure of nearby

215 point source, etc.) or weather patterns not frequently observed. Also, the availability of test data at some locations is weak (less than 50%), which can contribute to a poorer skill score.



220 **Figure 2:** Machine learning statistics between hourly observations and the corresponding bias-corrected model predictions for each observation location. Shown are the normalized mean bias (NMB), normalized root mean square error (NRMSE) and Pearson correlation coefficient (R) for the training data (blue) and the test data (red). Data sorted by region: China, Europe, United States (USA), and rest of the world (ROW). The mean values across all locations are shown in the figure inset.

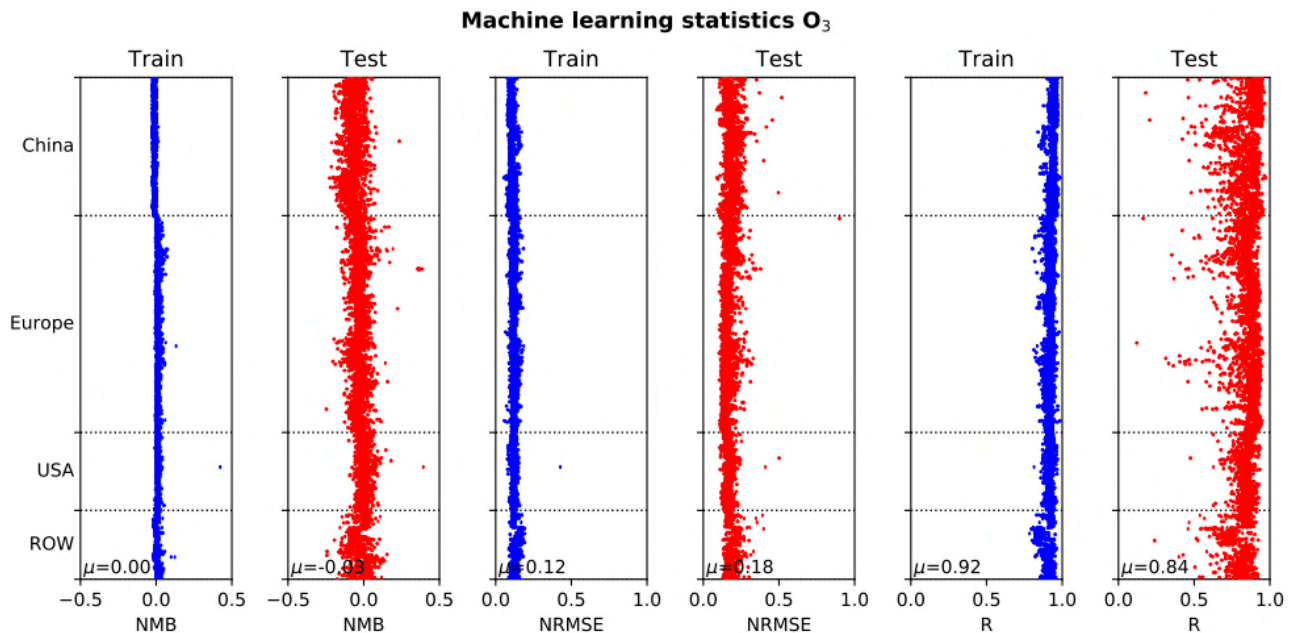


Figure 3: As Figure 2 but for O₃.

225 2.3.4 Uncertainty estimation

To quantify the uncertainty of an individual model predictions at any given site, we use the standard deviation of the model-observation differences on the test data. For sites with 100% test data coverage, this represents the standard deviation from a sample of 17,520 hourly model-observation pairs. The thus obtained individual NO₂ prediction uncertainties range between 3.9 – 28 ppbv (mean = 8.5 ppbv) at
230 polluted sites and 0.1 – 18 ppbv at clean sites (average of 4.9 ppbv). On a relative basis, this corresponds to an average uncertainty of 45% at polluted sites and 65% at clean sites. For O₃, we obtain an average individual prediction uncertainty of 14 ppbv (4.6 – 33 ppbv) at polluted sites and 9.0 ppbv (2.8 – 45 ppbv) at clean sites, corresponding to an average relative uncertainty of an individual prediction of 29% and 33% at polluted and clean sites, respectively.

235 The results presented in this paper are averages aggregated over multiple hours and locations, and the reported uncertainties are adjusted accordingly by calculating the mean uncertainty $\bar{\sigma}$ from the above-described hourly uncertainties σ_i :

$$\bar{\sigma}^2 = \sum_{i=1}^N \left(\frac{\sigma_i}{N}\right)^2$$

240 This assumes that the errors across individual sites are uncorrelated. The error covariance across sites is complex: two urban sites close to each other might show a low degree of error correlation due to local (street canyon etc) scale differences, whereas two background sites further apart might show significantly more correlation due to regional (synoptic) scale processes. In addition, our uncertainty
245 calculation also implies that the aggregated mean error approaches zero. Given that the average mean biases of the machine learning models are clustered around zero (Fig. 2 and Fig. 3), this is a valid general assumption - especially when aggregating across multiple sites. For simplicity we keep the current analysis, but acknowledge that it might lead to overly optimistic uncertainty estimates for sites with a relatively large mean bias.

250 2.4 Lockdown dates

To support interpretation and guide visualizations, we include approximate national lockdown dates in all figures. The start and end dates for these are from https://en.wikipedia.org/wiki/COVID-19_pandemic_lockdowns (as of July 1, 2020) or based on local knowledge, with the full list of start and
255 end dates given in Table A2. It should be noted that in many countries, lockdown policy varied regionally and many locations enacted ‘soft’ stay-at-home orders before the official lockdowns. Human behavior is therefore expected to have changed considerably in many locations before the official lockdowns went into force.

3 Results

260 3.1 Nitrogen dioxide

Figure 4 shows the weekly mean observations of NO₂ concentration, the GEOS-CF estimate and the BCM prediction based on the machine-learning predictor trained on 2018-2019 for the five cities of Wuhan (China), Taipei (Taiwan), Milan (Italy), New York (USA) and Rio de Janeiro (Brazil) from January 2018 through June 2020. We choose these five cities for illustration as they represent a diverse level of socio-economic development and due to the cities' variable responses to the COVID-19 pandemic. These five cities are also illustrative of the varying quality of the uncorrected GEOS-CF predictions compared to the observations. For example, as shown by the dashed grey lines vs. the solid black lines in Fig. 4, the uncorrected model predictions are in good agreement with observations in Rio de Janeiro but underestimate the observed NO₂ concentrations in Taipei and Milan while overestimating concentrations over New York. These differences are a combination of the observation-model scale mismatch (25x25 km² vs. point observation) and model errors, such as the simulated spatiotemporal distribution of NO_x emissions or the modelling of the local boundary layer. The model-observation mismatch is particularly pronounced for Wuhan, where the model does not capture the observed seasonal cycle, pointing to errors in the imposed seasonal cycle of NO_x emissions in the model.

275 In contrast to the uncorrected model predictions, the BCM closely follows the observations for years 2018 and 2019 (dashed black lines in Fig. 4). The grey region in Fig. 4 shows the start and end of the implementation of COVID-19 containment measures. Once containment is implemented, observed concentrations start to diverge from the BCM prediction for Wuhan, Milan and New York (Fig. 4). For 280 Wuhan, we find a reduction in NO₂ of 54 (48-59)% relative to the expected BCM value for February and March 2020, and average decreases of 30-40% are found over Milan (24-43%) and New York (20-34%) starting in mid-March and lasting through April (Fig. 4; Tables A3-A5). For cities where restrictions have been mainly removed (Wuhan, Milan) concentrations rise back towards the BCM value, although in neither city are the concentrations fully restored to what might be expected based on 285 the business-as-usual GEOS-CF simulation.

Looking more broadly at cities around the globe, 53 of the 64 specifically analysed cities feature NO₂ reductions of between 20-50% (Fig. A6-A8 and Tables A3-A5). Most locations issued social distancing recommendations prior to the legal lockdowns and observed NO₂ declines often precede the official 290 lockdown date by 7-14 days (e.g., Brussels, London, Boston, Phoenix, and Washington, DC).

For Taipei and Rio de Janeiro, the observations and the BCM show little difference (Fig. 4), consistent with the less stringent quarantine measures in these places. Other cities with only short-term NO₂ reductions of less than 25% include Atlanta (USA), Prague (Czech Republic), and Melbourne 295 (Australia), again fitting with the comparatively relaxed containment measures in these places (Fig. A6-A8). In contrast, Tokyo (Japan) and Stockholm (Sweden), which also implemented a less aggressive COVID-19 response, exhibit NO₂ reductions comparable to those of cities with official lockdowns (>20%), suggesting that economic and human activities were similarly subdued in those cities.

300 Substantial differences exist between cities in South America, with Rio de Janeiro and Santiago de
Chile showing little change thus far in 2020, whereas Quito (Ecuador) and Medellin (Colombia)
experienced a greater than 50% reduction in NO₂ after the initiation of strict restrictions measures in
mid-March (Fig. A8 and Table A5). Concentrations in Medellin rebounded sharply in April and May,
while concentrations in Quito remained 55 (52-58)% below business as usual throughout May and only
305 started to return back to normal in June.

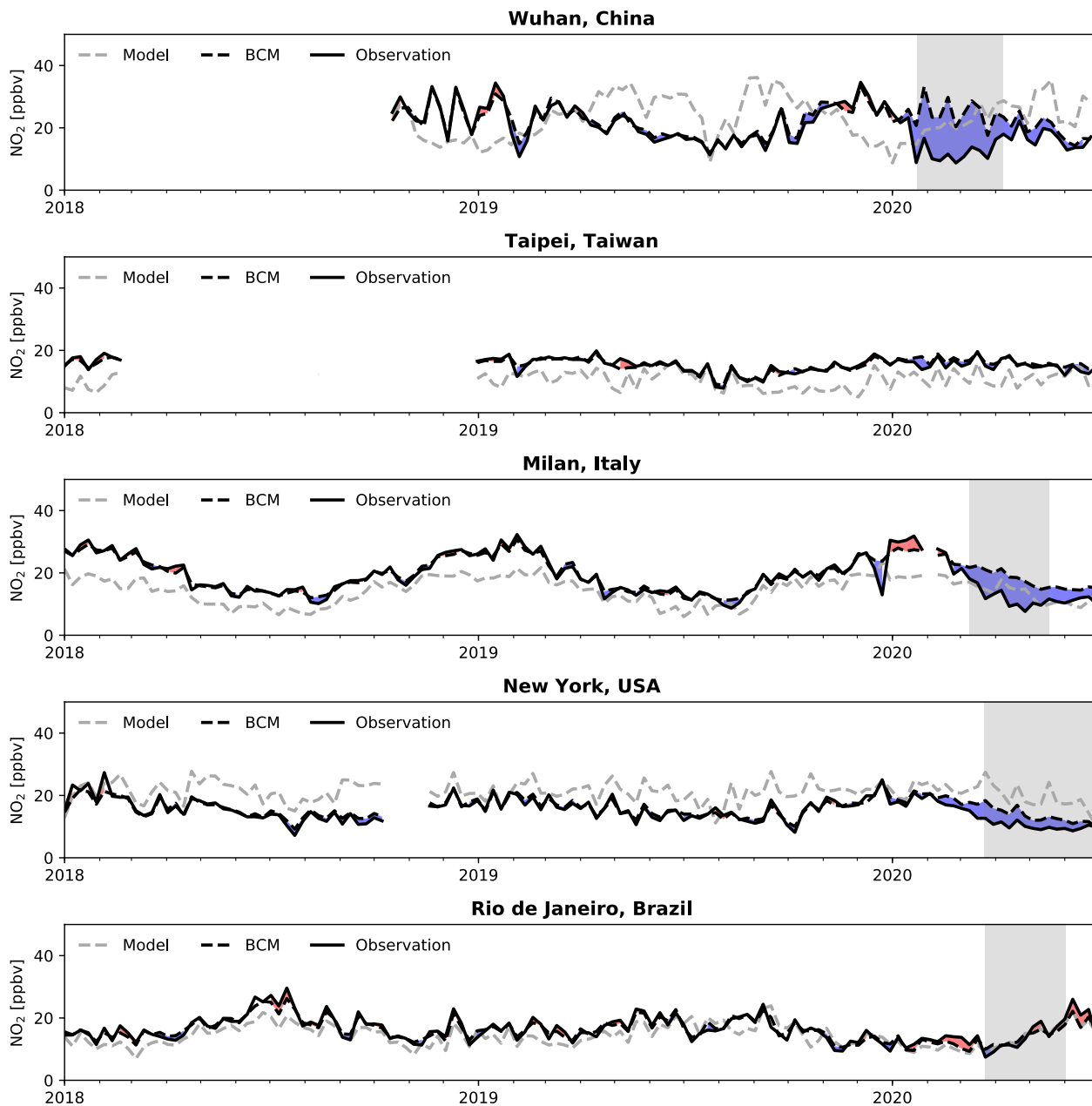


Figure 4. Comparison of NO₂ surface concentrations (ppbv = nmol mol⁻¹) for Wuhan, Taipei, Milan, New York, and Rio de Janeiro for January 2018 through June 2020. Observed values are shown in solid black, the original GEOS-CF model simulation is shown in dashed grey, and the BCM predictions are in dashed black. The area between observations and BCM predictions is shaded blue (red) if observations are lower (higher) than BCM predictions. Grey areas represent the period of lockdown. Shown are the 7-day average mean values for the 9, 18, 19, 14 and 2 observational sites in Wuhan, Taipei, Milan, New York, and Rio de Janeiro, respectively. Observations for China are only available starting in mid-September 2018.

315 To evaluate the large-scale impact of COVID-19 restrictions on air quality, we aggregate the individual
observation-model comparisons by country. We note that our estimates for some countries (e.g., Brazil,
Colombia) are based on a single city and likely not representative of the whole country. On a country
level, we find the sharpest and earliest drop in NO₂ over China, where observed concentrations fell, on
320 (Fig. 5). Concentrations remained at this level until late February, at which point they started to increase
until restrictions were significantly relaxed in early April. Our analysis suggests that Chinese NO₂
concentrations have recovered to within 5 (1-9)% of the business as usual since then. For 2019 (dashed
line in Fig. 5) the BCM shows a reduction in NO₂ concentrations around Chinese New Year (5th
February 2019), and it is likely that some reduction around the equivalent 2020 period (25th January
325 2020) would have occurred anyway. However, the 2020 reductions are significantly larger and more
prolonged than in 2019. Similar to China, India shows large reductions in NO₂ concentration (58 (49-
67)%) coinciding with the implementation of restrictions in mid-March (Fig. 5); however, NO₂
concentrations have not yet recovered by the end of June, reflecting the prolonged duration of lockdown
measures. Other areas of Asia, such as Hong Kong and Taipei, implemented smaller restrictions than
330 China or India and they show significantly smaller decreases (less than 20%).
For Europe and the United States, we find widespread NO₂ reductions averaging 22 (19-25)% in March
and 33 (30-36)% in April (Fig. 5). In some countries, recovery is evident as lockdown restrictions are
removed or lessened (e.g., Greece, Romania) but in 29 out of 36 countries, concentrations remain 20%
or more below the business-as-usual scenario throughout May and June.

335

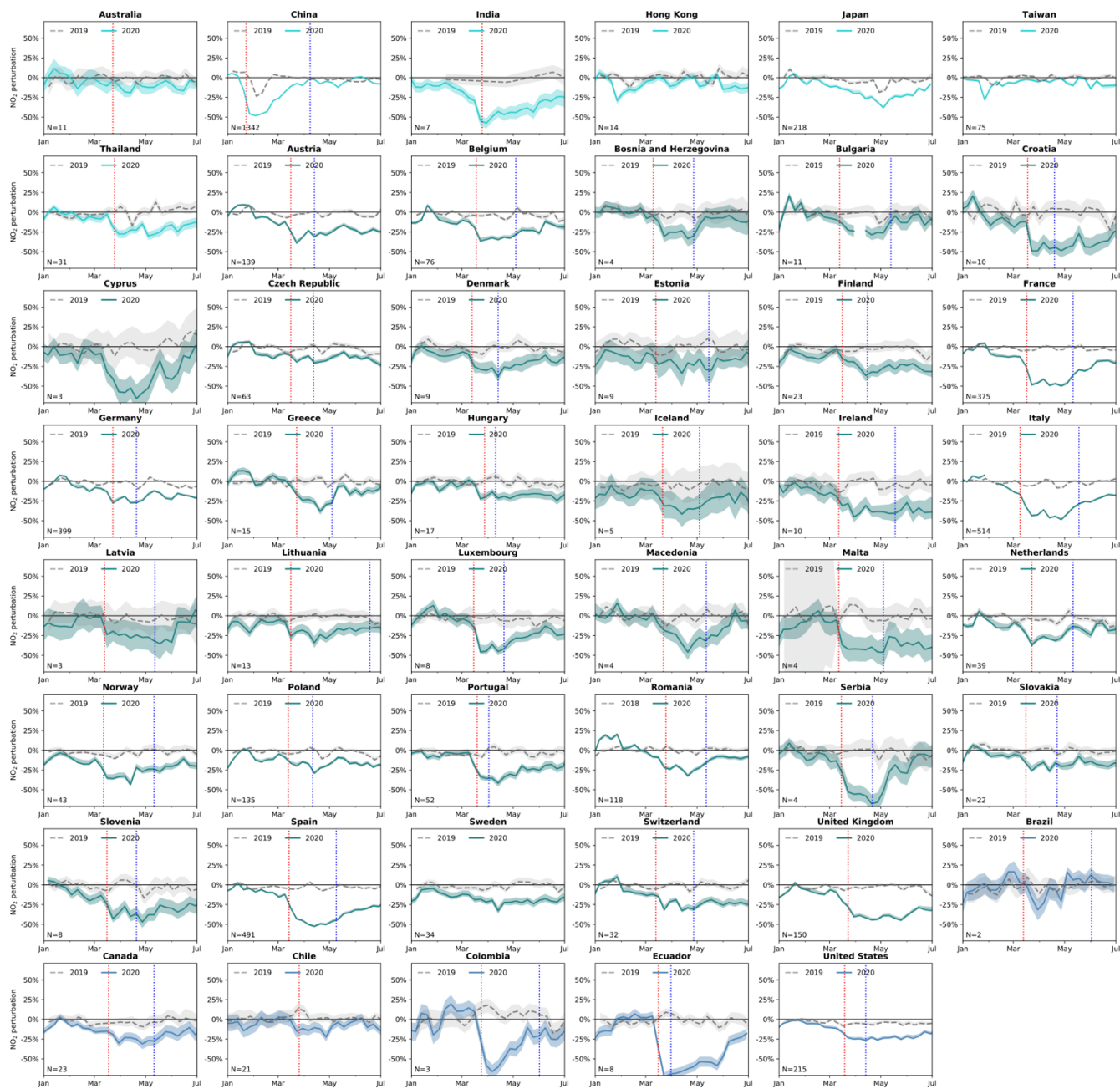


Figure 5: Seven-day average fractional difference between observed NO_2 and the BCM predictions for 46 countries between January 1 through June 30, aggregated from all sites across each country (number of sites in the bottom left of each panel). The thick line indicates the mean across all sites for the first half of 2020, with the shaded area representing the uncertainty estimate. Differing colours indicate differing regions (cyan: Asia & Australia; green: Europe; blue: Americas). The grey dashed line indicates the equivalent average for the same six month period in 2019 (note that 2019 data was included in the training). The red dashed vertical line indicates COVID-19 restriction dates, and the blue line indicates the beginning of easing measures.

3.2 Ozone

We follow the same methods for developing a business-as-usual counterfactual for O₃ as we did for NO₂ in section 3.1. Any change in local O₃ concentration arising from COVID-19 restrictions is set against a large seasonal increase in (background) concentrations in the Northern Hemisphere springtime (Fig. 6). Due to the longer atmospheric lifetime of O₃ compared to NO₂, the local O₃ signal is expected to be comparatively small. This makes attributing changes in O₃ concentration more challenging than for NO₂. Our analysis shows an O₃ increase of up to 50% for some periods in cities with large NO₂ reductions (e.g., Wuhan, Milan, Quito; Fig. 3 and Fig. A9-A11), but there is much less convincing evidence for a systematic O₃ response across cities or on a regional level (Fig. 7). For example, our analysis shows little O₃ difference in Beijing and Madrid during lockdown despite NO₂ declines comparable to Wuhan or Milan (Fig. A9-A11). O₃ enhancements of up to 20% are found over Europe (e.g., Belgium, Luxembourg, Serbia), with a peak in early April, approximately two weeks after lockdown started (Fig. 7).

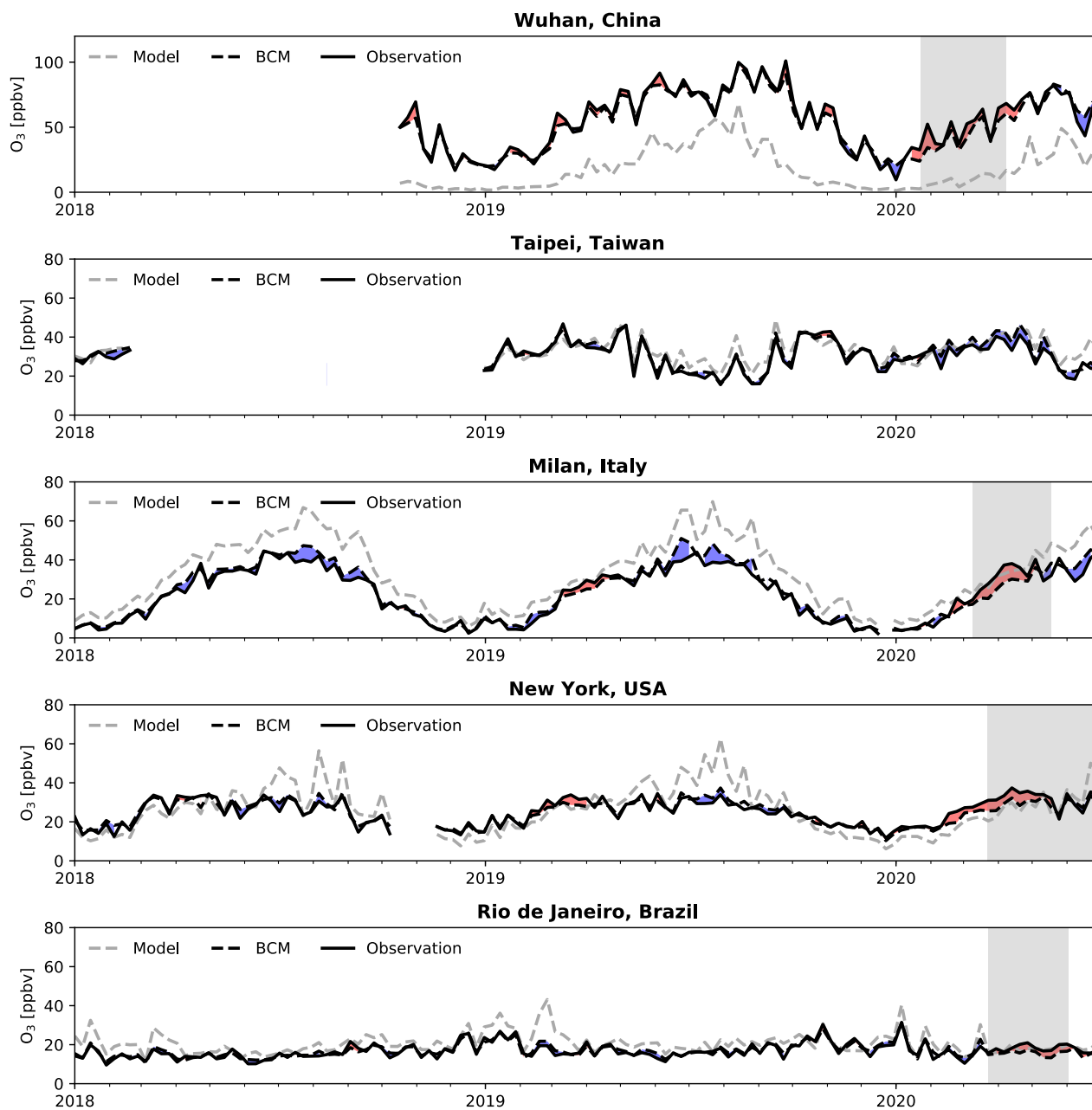
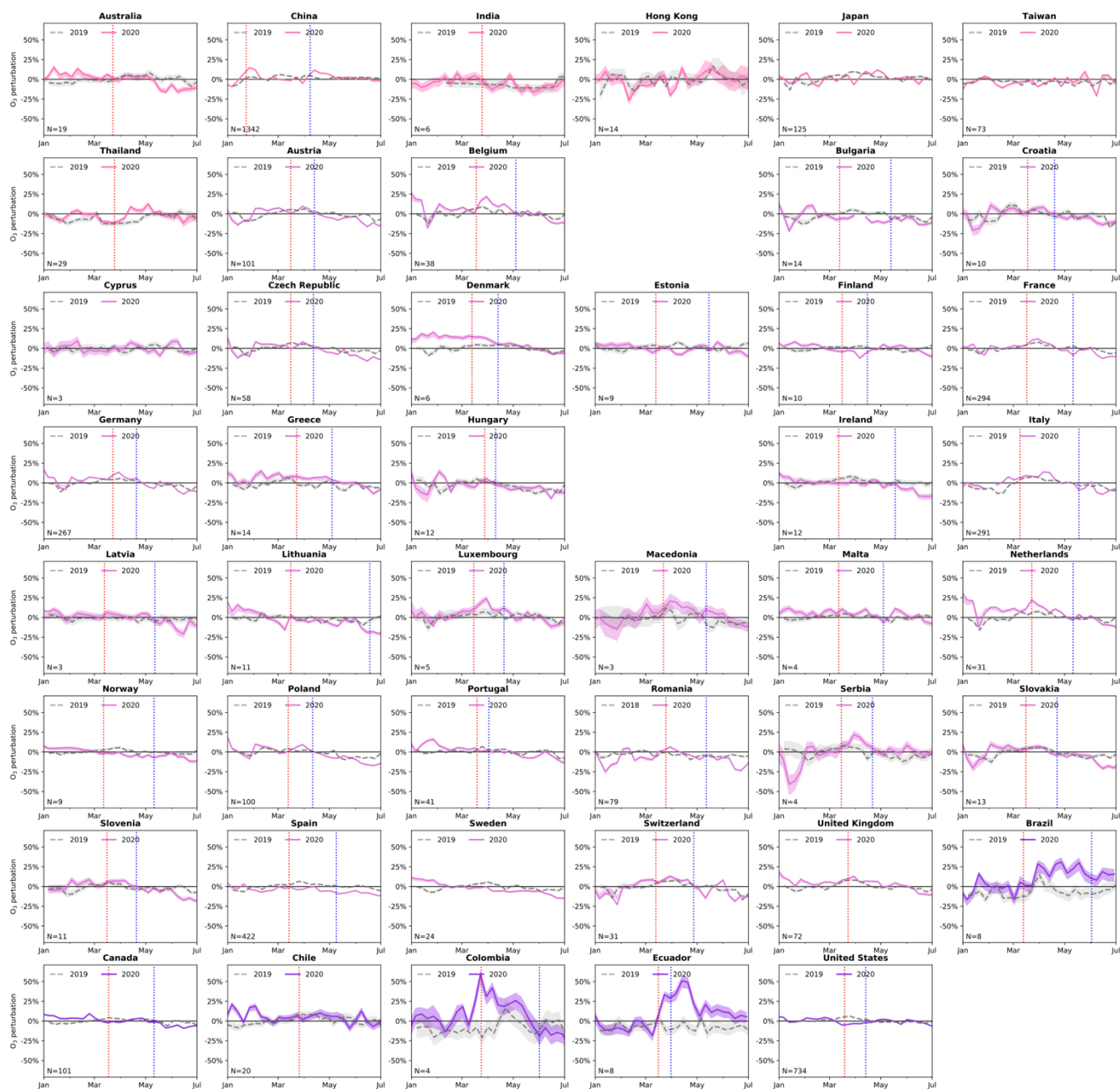


Figure 6: Comparison of O_3 surface concentrations for Wuhan, Taipei, Milan, New York, and Rio de Janeiro for January 2018 through June 2020. Observed values are shown in solid black, the original GEOS-CF model simulation is shown in dashed grey, and the BCM predictions are in dashed black. The area between observations and BCM predictions is shaded blue (red) if observations are lower (higher) than BCM predictions. The grey areas represent the period of lockdown. Shown are the 7-day average mean values for the 9, 18, 19, 14 and 4 observational sites in Wuhan, Taipei, Milan, New York, and Rio de Janeiro, respectively. Observations for China are only available starting in mid-September 2018.

360



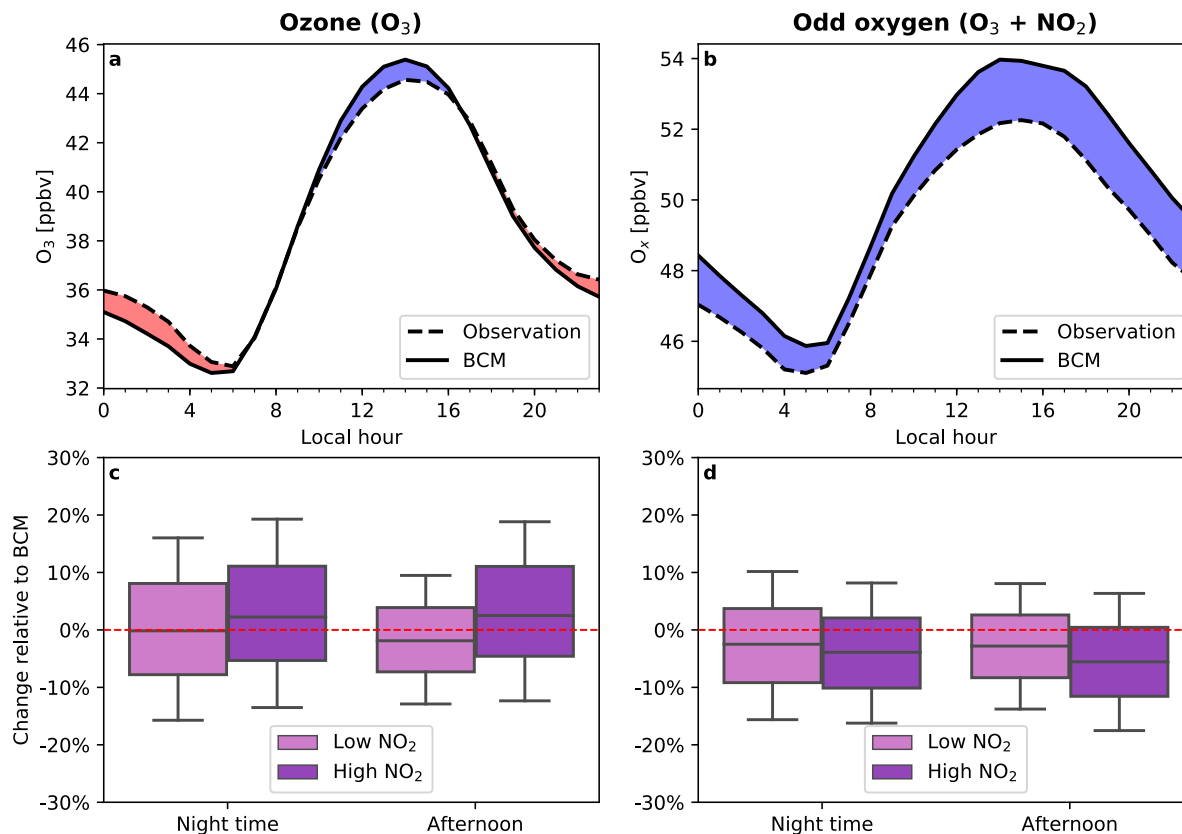
365 **Figure 7:** Similar to Figure 5 but for O_3 and without Bosnia and Herzegovina and Iceland. Differing colors indicate differing regions (pink: Asia & Australia; light purple: Europe; dark purple: Americas).

The analysis of O_3 is complicated by its nonlinear chemical response to NO_x emissions. In the presence of sunlight, O_3 is produced chemically from the oxidation of volatile organic compounds in the presence of NO_x (Seinfeld and Pandis, 2016). Therefore, a decline in NO_x emissions could decrease O_3 production and thus suppress O_3 concentrations. On the other hand, the process of NO_x titration, in
 370

which freshly emitted NO rapidly reacts with O₃ to form NO₂, acts as a sink for O₃ (Seinfeld and Pandis, 2016). Odd oxygen (O_x=NO₂+O₃) is conserved when O₃ reacts with NO and thus offers a tool for separating these competing processes. Figure 8 presents the global mean diurnal cycle for O₃ and O_x for the 5-month period since February 1, 2020 for both the observations and the BCM model, based on the individual hourly predictions at each observation site aggregated by local hour. The analysis of O₃ and O_x is based on the same set of observation sites where both NO₂ and O₃ observation are available (see Fig. 1). Compared to the BCM model, there has been an increase in the concentration of night time O₃ (midnight-5.00 local time, Fig. 8a) by 1 part per billion by volume (ppbv = nmol mol⁻¹) compared to the BCM, whereas O_x shows a decrease of 1 ppbv (Fig. 8b). While these changes are small in magnitude, they represent a multi-month aggregate over 3,485 observation sites that are statistically significant at the 1% confidence interval. It should be noted that the biases of the machine learning models show little diurnal variability (Fig. A12-13), suggesting that this result is not caused by poor model performance during specific times of the day.

Our results indicate that during the night, reduced NO emissions led to a reduction in O₃ titration, allowing O₃ concentrations to increase. During the afternoon, we find that O₃ concentrations are lower by 1 ppbv (Fig. 8a), while observed O_x concentrations are lower than the baseline model by almost 2 ppbv at 14:00 local time (Fig. 8b). We attribute the lower O_x to reduced net O_x production due to the lower NO_x concentration, but as titration is also reduced, daytime O₃ concentrations are little changed. Overall changes to mean O₃ concentrations are small, but there is a flattening of the diurnal cycle.

As shown in the lower panels in Fig. 8, both factors - enhanced night time O₃ and reduced daytime O_x - are more pronounced at locations where pre-existing NO₂ concentrations are high (> 15 ppbv). This suggests that the observed O₃ deviations from the BCM are indeed coupled to NO_x reductions due to COVID-19 restrictions, given that those are most pronounced at polluted sites.



395

Figure 8: Observed and BCM modelled diurnal cycle of O_3 (a) and O_x (b) averaged across all surface observation sites between February 1, 2020 through June 30, 2020 with estimated corresponding changes in surface O_3 (c) and O_x (d) relative to the BCM. Barplots (c and d) show observed changes during night time (0-5 local time) and the afternoon (12-17 local time) for locations with low (< 15 ppbv) and high (> 15 ppbv) NO_2 concentrations (based on the 2019 average).

400 3.3 NO_x emission reductions

The NO_2 analysis presented in Section 3.1 implies a stark reduction in NO_x emissions. However, due to the impact of atmospheric chemistry, changes in NO_2 concentrations do not reflect the same relative change in NO_x emissions. Because of this, the NO_2/NO_x ratio and the NO_x lifetime, both of which depend on seasonality and the local chemical environment, need to be taken into account when inferring NO_x emissions from NO_2 concentrations (Lamsal et al., 2011; Shah et al., 2020). To estimate the relationship between changes in NO_x emission and changes in NO_2 concentrations, we conducted a sensitivity simulation for the time period December 1, 2019 to June 8, 2020 using the GEOS-CF model with perturbed anthropogenic emissions. The perturbation simulation uses anthropogenic NO_x emissions scaled based on adjustment factors derived from NO_2 tropospheric columns observed by the NASA OMI instrument (Boersma et al., 2011). Daily scale factors were computed by normalizing coarse-resolution (2x2.5 degrees), 14-day NO_2 tropospheric column moving averages by the corresponding moving average for year 2018 (the emissions base year in GEOS-CF; section 2.2). Forest fire signals were filtered out based on QFED emissions and no scaling was applied over water. This

405

410

415 results in anthropogenic emission adjustment factors of 0.3 to 1.4 (Fig. A14), comparable to the
magnitude obtained from the observation-BCM comparisons at cities globally (Fig. 5) and capturing the
range of expected NO_x emission changes. However, it should be noted that the scale factors do not
necessarily coincide in space and time with the ones derived from observations and the BCM, and they
do not include any adjustment for the NO₂/NO_x ratio.

420 Figure 9a shows the response of NO₂ surface concentration to a change in NO_x emissions, derived from
the comparison of the sensitivity experiment against the GEOS-CF reference simulation. Our results
indicate that NO₂ concentrations drop, on average, by 80% of the fractional decrease in anthropogenic
NO_x emission, with a further diminishing effect for emission reductions greater than 50%. This reflects
both the buffering effect of atmospheric chemistry and the presence of natural background NO₂. The
425 here derived average sensitivity of 0.8 between a change in surface NO₂ to a change in NO_x emissions is
comparable to the value of 0.86 (1/1.16) obtained by Lamsal et al. (2011) for the relationship between
NO_x emissions and tropospheric column NO₂ observations.

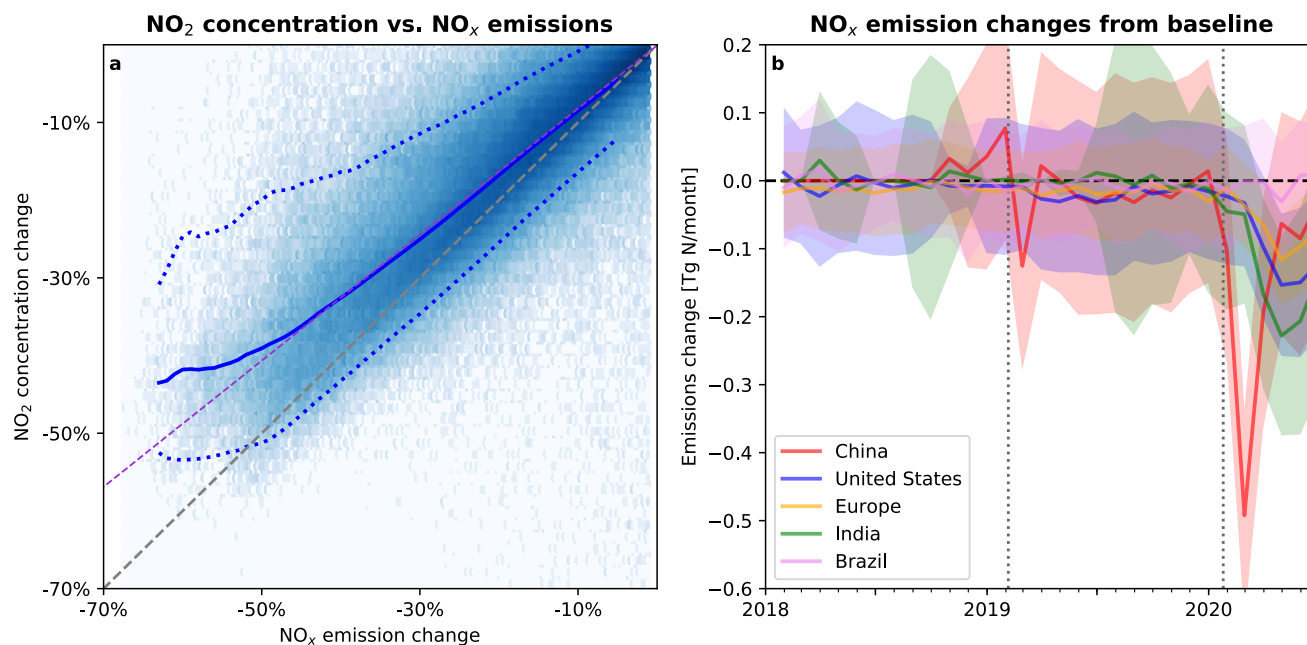
To infer the reduction in anthropogenic NO_x emissions due to COVID-19 containment measures during
430 the first six months of 2020, we use the best linear fit between the simulated NO_x/NO₂ sensitivity
(dashed purple line in Fig. 9a). To do so, we calculate the monthly percentage emission change at each
observation site based on the NO₂ anomalies derived in Section 3.1 and the corresponding best fit
NO_x/NO₂ sensitivity (Fig. 9a). This is a simplification as the local NO_x/NO₂ sensitivity ratio is highly
dependent on the local environment. To account for this uncertainty, we assign an absolute error of 15%
435 to our NO_x/NO₂ sensitivity, as derived from the spread in the NO_x/NO₂ ratio in the sensitivity
simulation (Fig. 9a). We then aggregate these estimates to a country-level by weighting them based on
average NO₂ concentrations per location, thus giving higher weight to locations with more nearby NO_x
emission sources. It should be noted that for some countries, our estimates are based upon a small
number of observation sites that might not be representative for the country as a whole. This is
440 particularly true for India and Brazil, where less than 10 observation sites are available. While the
smaller observation sample size is reflected in the wider uncertainty associated with these emission
estimates compared to countries with a much denser monitoring network (e.g., China or Europe), the
applied extrapolation method might incur errors that are not reflected in the stated uncertainty ranges.
To obtain absolute estimates in emission changes, the monthly country-level percentage emission
445 changes are convoluted with bottom-up emissions estimates for 2015 from the Emission Database for
Global Atmospheric Research (EDGAR v5.0_AP, Crippa et al., 2018, 2020). The choice of EDGAR
v5.0 as the bottom-up reference inventory (over e.g., the HTAP emissions inventory used in GEOS-CF)
was motivated by the fact that its baseline has been updated more recently and the country emission
totals - which our analysis is based on - are readily available.

450 As summarized in Table 2, we calculate that the total reduction in anthropogenic NO_x emissions due to
COVID-19 containment measures during the first six months of 2020 amounted to 3.1 (2.6-3.6) TgN
(Fig. 9b and Table 2). This is equivalent to 5.5 (4.7-6.4)% of global annual anthropogenic NO_x
emissions (Table 2). Our estimate encompasses 46 countries that together account for 67% of the total
455 emissions (excluding international shipping and aviation). We have no information for significant

countries such as Russia, Indonesia, or anywhere in Africa due to the lack of publicly available near real-time air quality information. China accounts for the largest fraction of the total deduced emission reductions (28%), followed by India (25%), the United States (18%), and Europe (12%).

460 While our method does not allow for sector-specific emission attribution, we assume our results to be most representative for changes in traffic emissions (rather than, say, aircraft emissions) given the location of the observation sites. On average, traffic emissions represent 27% of total anthropogenic NO_x emissions (Crippa et al., 2018), and our derived total NO_x emission reduction from Jan-Jun 2020 corresponds to 21 (17-24)% of global annual traffic emissions. The share of transportation on total NO_x emissions is higher in the US and Europe (approx.. 40%) compared to India and China (20-25%).

465 Taking this into account, the derived ratio of NO_x emission reductions to annual traffic emissions is 21 (16-26)% in the US, 25 (20-30)% in Europe, 39 (34-44)% in China, and 62 (55-69)% in India.



470 **Figure 9:** a) Response of NO₂ surface concentration (y-axis) to a change in NO_x emissions (x-axis), as deduced from a model sensitivity simulation (see methods). The solid blue line shows the mean value across all individual grid cells (blue squares) and the dotted blue lines show the 5% and 95% quantiles. The dashed purple line shows the best linear fit. b) Estimated monthly change in NO_x emissions from the baseline since 2018 for China (red), United States (blue), Europe (yellow), India (green), and Brazil (purple), as estimated from observed NO₂ concentration anomalies. Shaded areas indicate estimated emission uncertainties. Dotted grey lines indicate Chinese New Year 2019 and 2020.

475

Table 2: Anthropogenic NO_x emission reductions in GgN month⁻¹ as derived from NO₂ concentration changes.

	Baseline ¹	Feb-20	Mar-20	Apr-20	May-20	Jun-20
Australia	621	-2.9 (-13.8-8.0)	-3.7 (-14.4-6.9)	-8.5 (-18.5-1.6)	-6.1 (-16.1-3.8)	-7.9 (-17.6-1.8)
Austria	73	-0.5 (-1.4-0.5)	-1.7 (-2.7--0.7)	-2.0 (-3.0--1.0)	-1.6 (-2.6--0.6)	-1.8 (-2.8--0.8)
Belgium	98	-1.0 (-2.4-0.3)	-2.0 (-3.4--0.7)	-3.2 (-4.5--1.9)	-2.4 (-3.8--1.1)	-1.8 (-3.2--0.5)
Bosnia and Herzegovina	32	0.05 (-0.47-0.57)	-0.43 (-0.96-0.11)	-0.90 (-1.45--0.35)	-0.39 (-0.99-0.21)	-0.28 (-0.92-0.35)
Brazil	1844	-1.3 (-35.7-33.2)	-1.5 (-37.0-34.0)	-32.0 (-67.2-3.2)	7.2 (-26.1-40.6)	10.3 (-21.7-42.3)
Bulgaria	46	-0.12 (-0.83-0.58)	-0.60 (-1.32-0.12)	-1.20 (-1.93--0.46)	-0.67 (-1.44-0.11)	-0.41 (-1.20-0.37)
Canada	755	-6.3 (-17.1-4.6)	-12.2 (-23.3--1.1)	-19.8 (-31.4--8.1)	-18.5 (-30.5--6.5)	-11.4 (-23.8-1.0)
Chile	202	-0.5 (-3.9-2.9)	-0.7 (-4.0-2.6)	-2.8 (-6.0-0.4)	-1.6 (-4.7-1.4)	-1.0 (-4.1-2.1)

China	11876	-517 (-669--366)	-191 (-342--39)	-63 (-215-89)	-82 (-235-70)	-30 (-182-123)
Colombia	207	1.2 (-2.5-4.9)	-0.2 (-3.8-3.4)	-12.0 (-15.5--8.5)	-5.5 (-9.1--1.9)	-4.4 (-8.0--0.7)
Croatia	24	-0.25 (-0.64-0.14)	-0.55 (-0.95--0.15)	-1.03 (-1.44--0.63)	-0.96 (-1.37--0.55)	-0.90 (-1.31--0.48)
Czech Republic	108	-1.0 (-2.5-0.4)	-1.3 (-2.8-0.2)	-1.8 (-3.2--0.3)	-1.3 (-2.8-0.2)	-1.6 (-3.1--0.1)
Denmark	48	-0.5 (-1.3-0.3)	-0.8 (-1.6--0.1)	-1.4 (-2.1--0.6)	-1.0 (-1.8--0.2)	-0.8 (-1.5--0.0)
Ecuador	133	0.5 (-1.6-2.6)	-3.8 (-5.9--1.8)	-8.9 (-11.0--6.9)	-7.5 (-9.6--5.4)	-4.0 (-6.1--2.0)
Estonia	13	-0.20 (-0.44-0.05)	-0.16 (-0.41-0.10)	-0.28 (-0.54--0.02)	-0.29 (-0.54--0.03)	-0.20 (-0.45-0.04)
Finland	77	-1.1 (-2.3-0.1)	-0.8 (-2.0-0.4)	-2.3 (-3.6--1.1)	-2.0 (-3.3--0.8)	-2.0 (-3.3--0.8)
France	337	-3.2 (-7.6-1.2)	-9.1 (-13.5--4.7)	-15.7 (-20.1--11.3)	-12.7 (-17.1--8.2)	-6.9 (-11.3--2.4)
Germany	494	-3.0 (-9.4-3.4)	-7.1 (-13.5--0.7)	-11.5 (-17.9--5.1)	-8.3 (-14.7--1.9)	-9.2 (-15.7--2.8)
Greece	101	0.1 (-1.4-1.5)	-0.5 (-1.9-1.0)	-2.9 (-4.4--1.5)	-1.5 (-3.0--0.0)	-1.3 (-2.8-0.1)
Hong Kong	90	-1.5 (-2.8--0.2)	-0.2 (-1.6-1.1)	-0.4 (-1.7-1.0)	-0.3 (-1.6-1.0)	-1.2 (-2.6-0.2)
Hungary	55	-0.3 (-1.1-0.5)	-0.4 (-1.2-0.4)	-1.0 (-1.8--0.2)	-1.0 (-1.8--0.1)	-1.0 (-1.9--0.2)
Iceland	2	-0.04 (-0.08-0.01)	-0.04 (-0.09-0.01)	-0.09 (-0.14--0.04)	-0.07 (-0.12--0.01)	-0.04 (-0.10-0.01)
India	4693	-52 (-125-21)	-161 (-234--88)	-232 (-307--157)	-202 (-280--125)	-140 (-220--59)
Ireland	35	-0.3 (-1.0-0.3)	-0.8 (-1.4--0.2)	-1.3 (-1.9--0.7)	-1.4 (-2.0--0.8)	-1.2 (-1.8--0.6)
Italy	357	-1.9 (-6.5-2.7)	-9.7 (-14.4--5.1)	-15.6 (-20.2--10.9)	-12.4 (-17.1--7.8)	-7.7 (-12.3--3.0)
Japan	996	-4.1 (-17.2-9.0)	-12.6 (-25.7-0.6)	-23.4 (-36.7--10.2)	-28.7 (-41.9--15.4)	-18.0 (-31.3--4.7)
Latvia	14	-0.08 (-0.38-0.22)	-0.16 (-0.45-0.12)	-0.37 (-0.67--0.06)	-0.44 (-0.74--0.13)	-0.18 (-0.48-0.12)
Luxembourg	12	-0.17 (-0.48-0.15)	-0.27 (-0.58-0.05)	-0.50 (-0.82--0.18)	-0.40 (-0.72--0.07)	-0.32 (-0.64-0.01)
Lithuania	20	0.01 (-0.18-0.19)	-0.23 (-0.42--0.05)	-0.47 (-0.65--0.29)	-0.31 (-0.49--0.13)	-0.23 (-0.42--0.05)
Macedonia	10	-0.00 (-0.17-0.16)	-0.08 (-0.25-0.09)	-0.33 (-0.50--0.16)	-0.28 (-0.46--0.10)	-0.06 (-0.24-0.12)
Malta	3	-0.00 (-0.06-0.06)	-0.07 (-0.13--0.01)	-0.13 (-0.20--0.07)	-0.11 (-0.18--0.05)	-0.11 (-0.18--0.05)
Netherlands	121	-1.4 (-3.1-0.4)	-2.6 (-4.3--0.8)	-3.4 (-5.1--1.7)	-2.1 (-3.9--0.4)	-2.0 (-3.8--0.2)
Norway	63	-0.8 (-1.7-0.0)	-1.5 (-2.4--0.6)	-1.9 (-2.8--1.0)	-1.5 (-2.5--0.6)	-1.1 (-2.0--0.2)
Poland	284	-3.3 (-7.1-0.5)	-3.2 (-7.0-0.5)	-5.9 (-9.7--2.1)	-4.0 (-7.8--0.2)	-5.1 (-9.0--1.3)
Portugal	70	-0.4 (-1.4-0.6)	-1.2 (-2.2--0.2)	-2.6 (-3.6--1.5)	-1.9 (-2.9--0.9)	-1.6 (-2.6--0.5)
Romania	102	0.5 (-0.9-1.8)	-1.1 (-2.5-0.3)	-2.5 (-3.9--1.2)	-1.6 (-3.0--0.2)	-1.0 (-2.4-0.4)
Serbia	63	-0.48 (-1.54-0.59)	-1.77 (-2.87--0.68)	-3.83 (-4.94--2.72)	-2.24 (-3.44--1.04)	-0.82 (-2.07-0.43)
Slovakia	33	-0.20 (-0.67-0.28)	-0.43 (-0.90-0.05)	-0.61 (-1.09--0.13)	-0.54 (-1.04--0.05)	-0.57 (-1.07--0.07)
Spain	333	-2.9 (-7.2-1.5)	-8.6 (-13.0--4.2)	-17.0 (-21.3--12.6)	-13.9 (-18.3--9.5)	-10.0 (-14.5--5.6)
Sweden	85	-1.0 (-2.2-0.2)	-1.3 (-2.5--0.0)	-2.0 (-3.3--0.8)	-1.9 (-3.1--0.6)	-1.6 (-2.9--0.4)
Switzerland	36	-0.25 (-0.77-0.26)	-0.65 (-1.16--0.14)	-0.94 (-1.45--0.43)	-0.83 (-1.36--0.30)	-0.84 (-1.37--0.31)
Taiwan	371	-3.7 (-8.6-1.2)	-1.5 (-6.4-3.5)	-1.3 (-6.2-3.7)	-1.7 (-6.7-3.4)	-3.9 (-8.9-1.2)
Thailand	458	-2.6 (-9.2-4.0)	-4.8 (-11.7-2.0)	-10.7 (-17.6--3.8)	-11.6 (-18.6--4.7)	-8.5 (-15.6--1.4)
United Kingdom	390	-3.0 (-8.3-2.2)	-6.8 (-12.0--1.6)	-16.4 (-21.6--11.2)	-16.4 (-21.6--11.1)	-12.8 (-18.0--7.5)
United States	6243	-34 (-116-48)	-94 (-177--11)	-155 (-239--72)	-147 (-231--64)	-123 (-207--40)
Other countries ²	1307	n/a	n/a	n/a	n/a	n/a
Shipping and Aviation	671	n/a	n/a	n/a	n/a	n/a
Total	4681	-651 (-843--460)	-553 (-745--360)	-692 (-885--498)	-603 (-798--408)	-418 (-615--222)

¹ EDGAR v5.0 AP 2015 annual emissions expressed as GgN month⁻¹ (Crippa et al., 2020)

² Primarily Indonesia, Iran, Mexico, Pakistan, Russia, Saudi Arabia, South Africa, South Korea, Vietnam

3.4 Long-term impact of reduced NO_x emissions on surface O₃

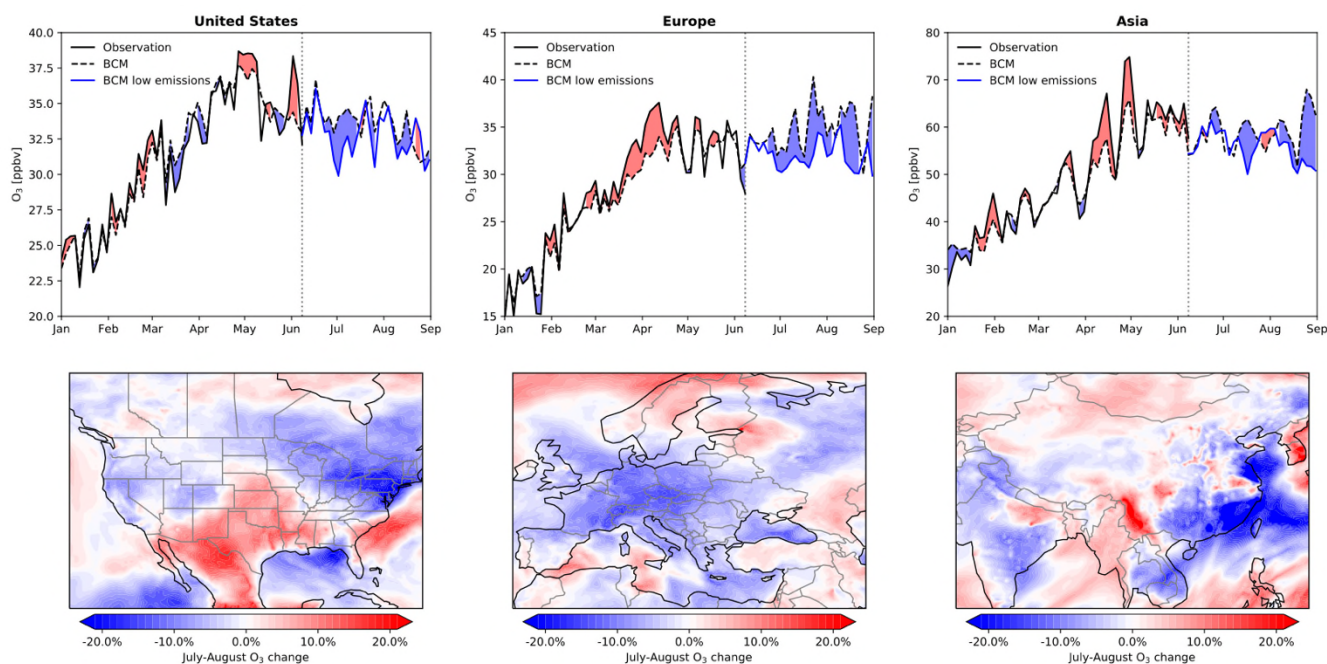
480 The response of O₃ to NO₂ declines in the wake of the COVID-19 outbreak is complicated by the competing influences of atmospheric chemistry. From February through June 2020, the diurnal observation-BCM comparisons suggest that the reduction in photochemical production was offset by a smaller loss from titration, as described in Section 3.2. This resulted in a flattening of the diurnal cycle and an insignificant net change in surface O₃ over a diurnal cycle. The competing impacts of reduced

485 NO_x emissions on O₃ production and loss are dependent on the local chemical and meteorological environment. This is reflected in the variable geographical response of O₃ following the implementation of COVID-19 restrictions (Le et al., 2020; Dantas et al., 2020). Moreover, as atmospheric reactivity

increases through the Northern Hemisphere spring and summer, the relative importance of photochemical production is expected to increase in the Northern Hemisphere.

490 To assess the potential seasonal-scale impact of reduced anthropogenic emissions on O₃, we conducted two free-running forecast simulations between June 8 through August 31, 2020, initialized from the GEOS-CF simulation and the sensitivity simulation described in Section 3.3, respectively. Both simulations use the same biomass burning emissions based on a historical QFED climatology. For the forecast sensitivity experiment, we assume a sustained, time-invariant 20% reduction in global anthropogenic emissions of NO_x, carbon monoxide (CO), and VOCs. We chose to alter not only the anthropogenic emissions of NO_x but also of other pollutants whose anthropogenic emissions are highly correlated to NO_x, as a reduction in NO_x emissions without corresponding declines in CO and VOC emissions seems unrealistic.

Figure 10 shows the differences between the reference forecast and the sensitivity simulation over the United States, Europe and China. Our results indicate that sustained lower anthropogenic emissions lead to a general decrease in surface O₃ concentrations of 10-20% over Eastern China, Europe, and the Western and Northeast US during July and August relative to the business-as-usual reference forecast simulation. However, it is also notable that in some locations the model forecast O₃ concentrations increase by an equivalent amount (e.g., Scandinavia, South Central US and Mexico, Northern India), reflecting the high nonlinearity of atmospheric chemistry. This highlights the complex interactions between emissions, chemistry, and meteorology and their impact on air pollution on different time scales.



510 **Figure 10:** Change in mean surface O₃ over the United States, Europe, and Asia for a sensitivity simulation with altered anthropogenic emissions. Top panels show daily average O₃ concentrations at all observation sites within the given region (solid black, Jan-Jun), the bias-corrected GEOS-CF model (“BCM”, solid black, Jan 1st - Jun 8th) continued with a business-as-usual GEOS-CF forecast from Jun 9th - Aug 31st, and GEOS-CF forecast assuming sustained 20% anthropogenic emission reduction (blue). Bottom panels show mean changes in surface O₃ for July and August for the low emissions simulation relative to the business-as-usual forecast.

4 Conclusions

515 The combined interpretation of observations and model simulations using machine learning can be used
to remove the compounding effect of meteorology and atmospheric chemistry, offering an effective tool
to monitor and quantify changes in air pollution in near real-time. The global response to the COVID-19
pandemic presents a perfect testbed for this type of analysis, offering insights into the
interconnectedness of human activity and air pollution. While national mitigation strategies have led to
520 substantial regional NO₂ concentration decreases over the past decades in many places (e.g., Hilboll et
al., 2013; Russell et al., 2013; Castellanos and Boersma, 2012), the widespread and near-instantaneous
reduction in NO₂ following the implementation of COVID-19 containment measures indicates that there
is still large potential to lower human exposure to NO₂ through reduction of anthropogenic NO_x
emissions.

525 The here derived NO₂ reductions are in good agreement with other emerging estimates. For instance, we
determine an 18% decline over China for the 20 days after Chinese New Year relative to the preceding
20 days, consistent with the 21% reduction reported in Liu et al. (2020a). Similarly, our estimated 22%
reduction over China for January to March 2020 is in excellent agreement with the 21-23% reported by
530 Liu et al. (2020b). For Spain, we obtain an NO₂ reduction of 46% between March 14 to April 23, again
in close agreement with the values reported in Petetin et al. (2020).

While large reductions in NO₂ concentrations are achievable and immediately follow curtailments in
NO_x emissions, the O₃ response is more complicated and can be in the opposite direction, at times by as
535 much as 50% (Jhun et al., 2015, Le et al., 2020). The O₃ response is dependent on season, time scale,
and environment, with an overall tendency to lower surface O₃ under a scenario of sustained NO_x
emission reductions. This shows the complexities faced by policy makers in curbing O₃ pollution.

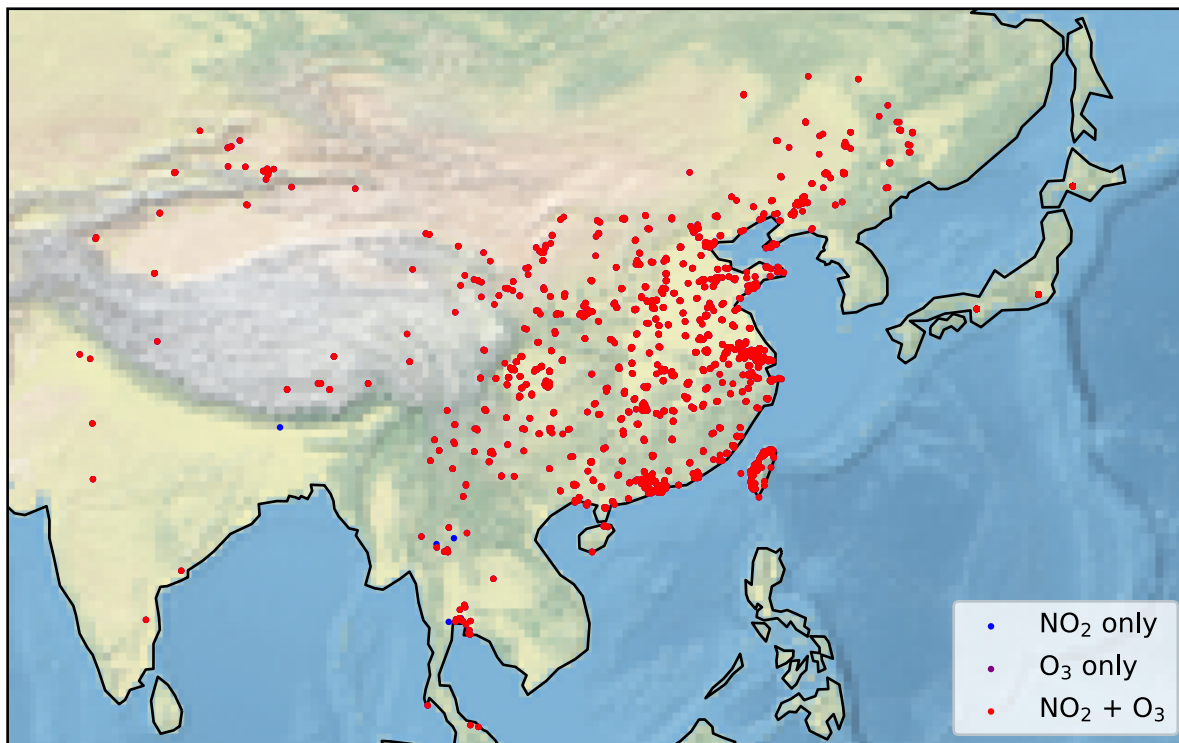


Figure A1: Close up of Chinese observation sites included in the analysis. Red points indicate sites with both NO₂ and O₃ observations, purple points show locations with O₃ observations only and blue points show locations with NO₂ observations only.

545

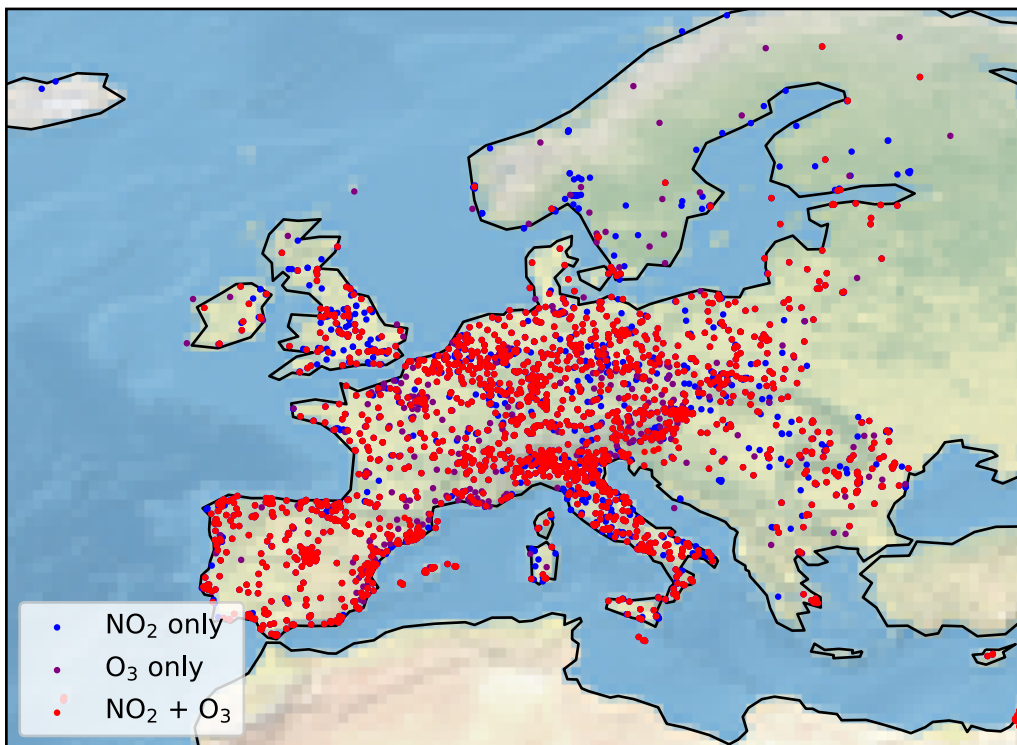
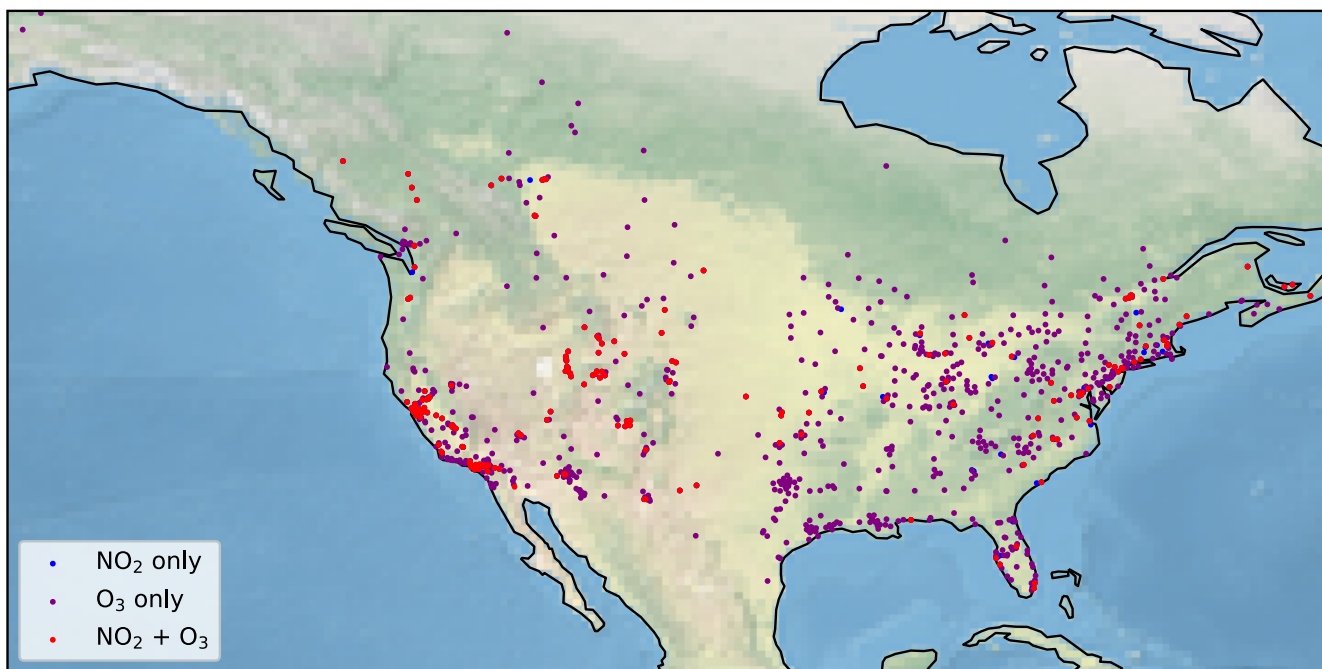
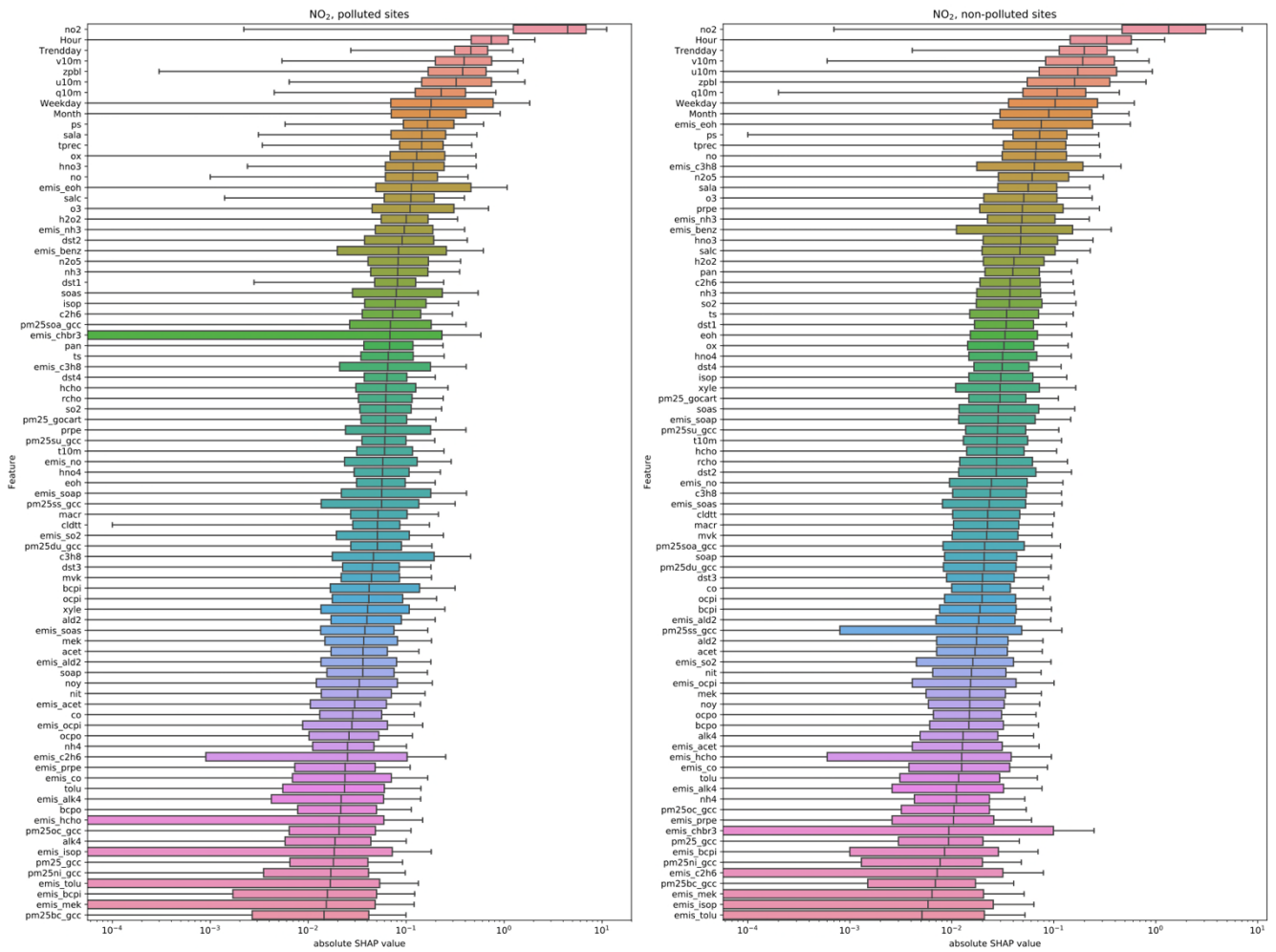


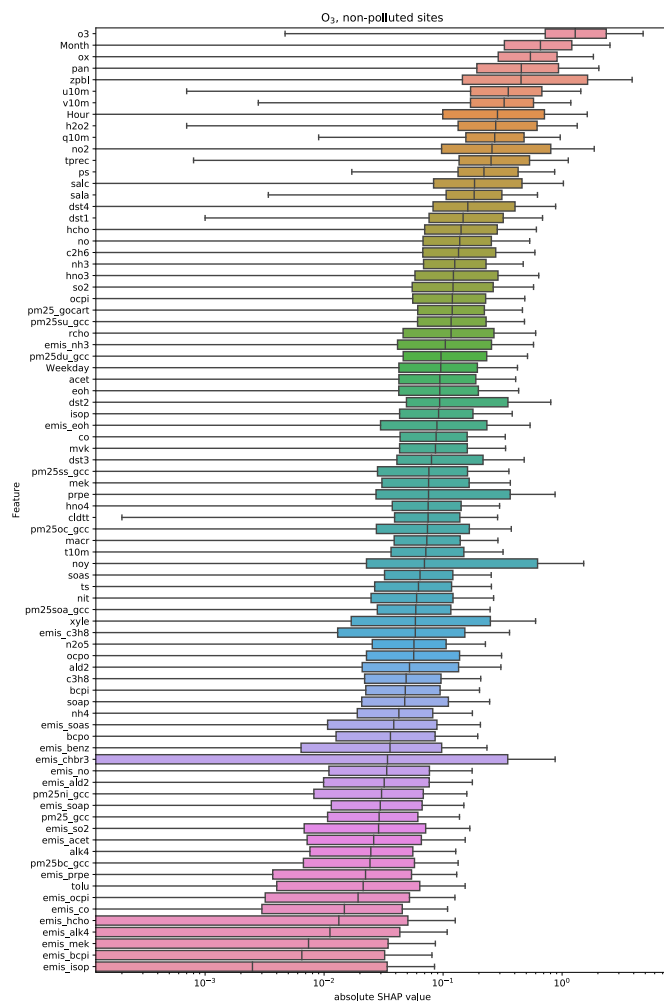
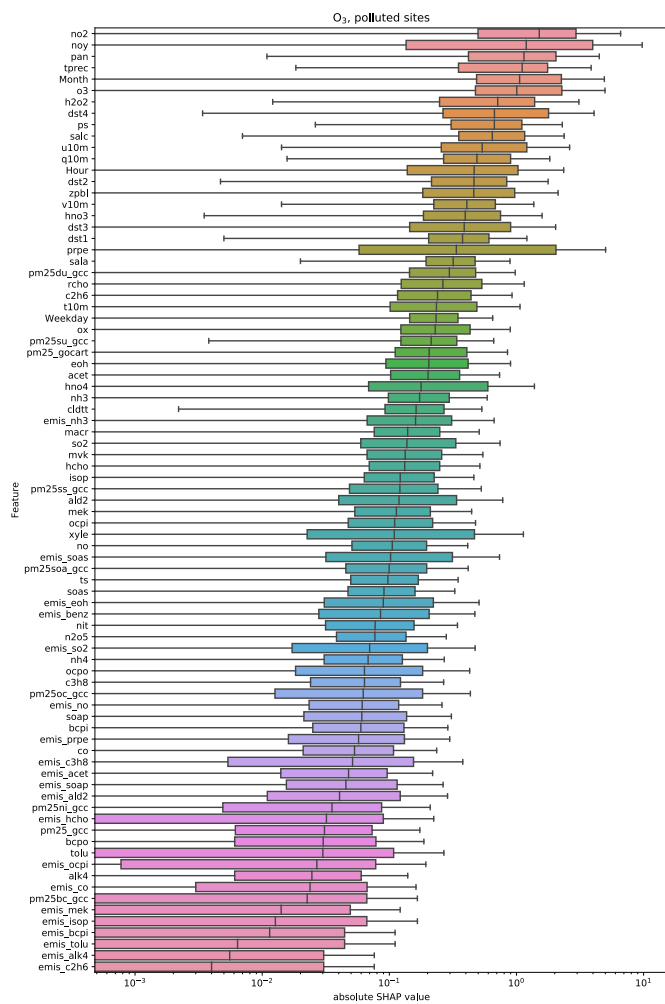
Figure A2: Close up of European observation sites included in the analysis. Red points indicate sites with both NO₂ and O₃ observations, purple points show locations with O₃ observations only and blue points show locations with NO₂ observations only.



550 **Figure A3:** Close up of North American observation sites included in the analysis. Red points indicate sites with both NO₂ and O₃ observations, purple points show locations with O₃ observations only and blue points show locations with NO₂ observations only.



555 **Figure A4:** Importance of input variables (features) for the XGBoost models trained to predict NO₂ model bias. Shown are the distribution of the absolute SHAP values for each feature, ranked by the average importance of each feature. Higher SHAP value indicates higher feature importance. Left panel shows results for polluted sites (average annual NO₂ concentration > 15ppbv) and right panel shows results for all other sites.



560

Figure A5: As Figure A4 but for O₃.

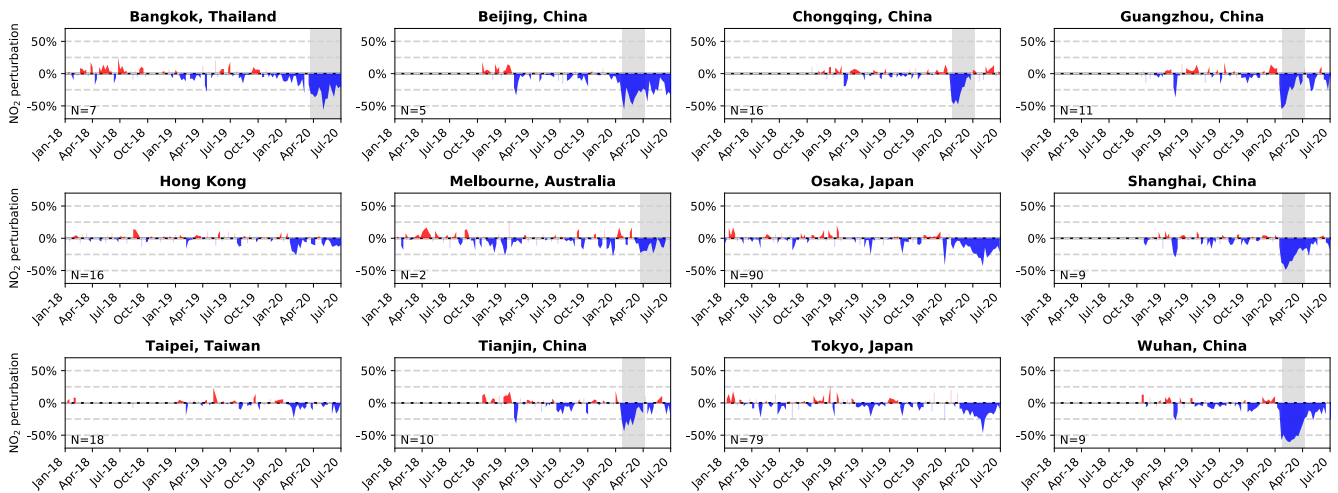


Figure A6: Normalized fractional NO₂ perturbations (observation - bias-corrected model, normalized by the bias-corrected model prediction) from Jan 1, 2018 through June 2020 for selected cities in Asia and Australia. Grey shaded areas indicate COVID-19 lockdown periods. Number of sites per city are shown in the bottom left of each panel.

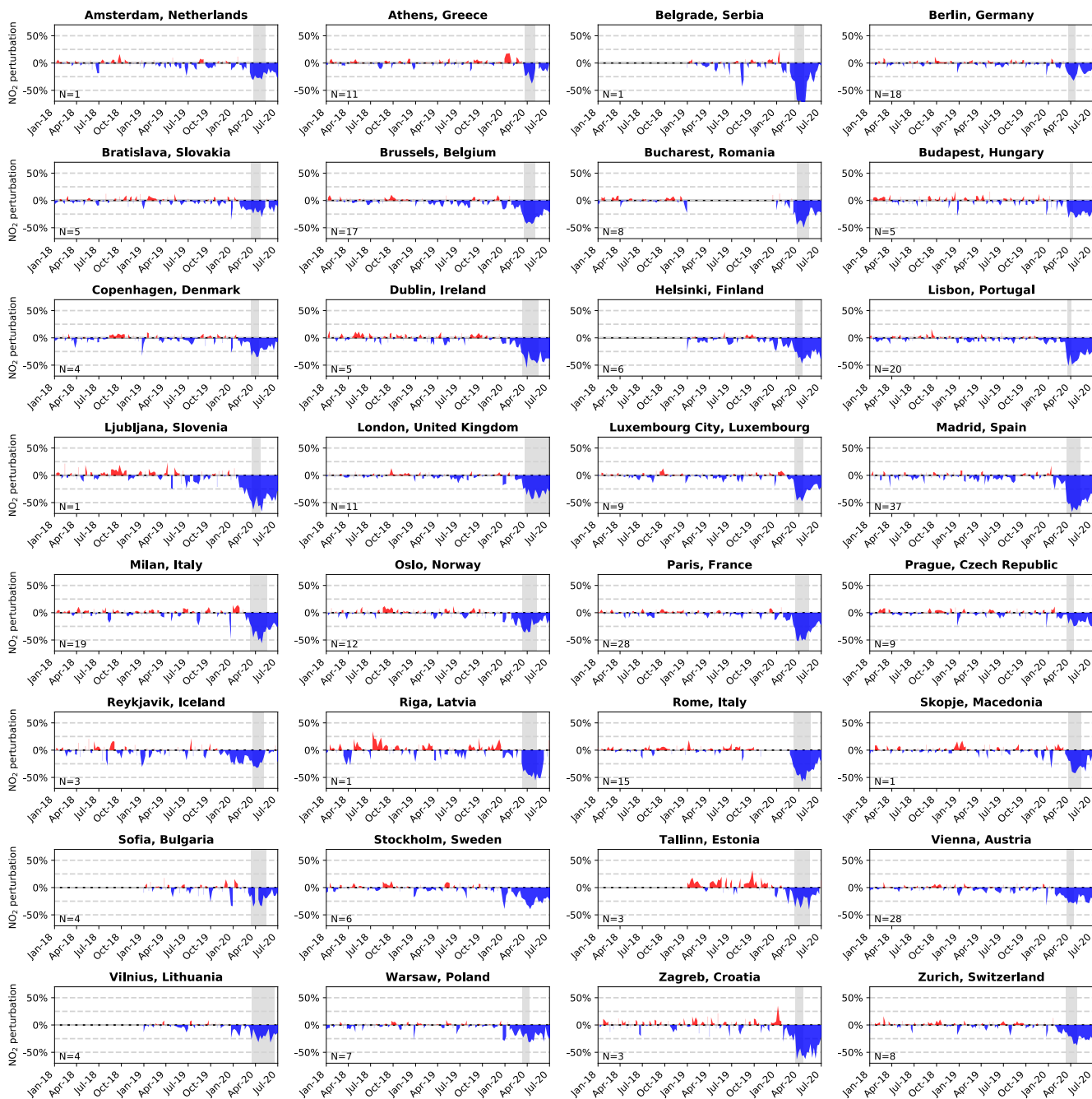


Figure A7: As figure A6 but for Europe.

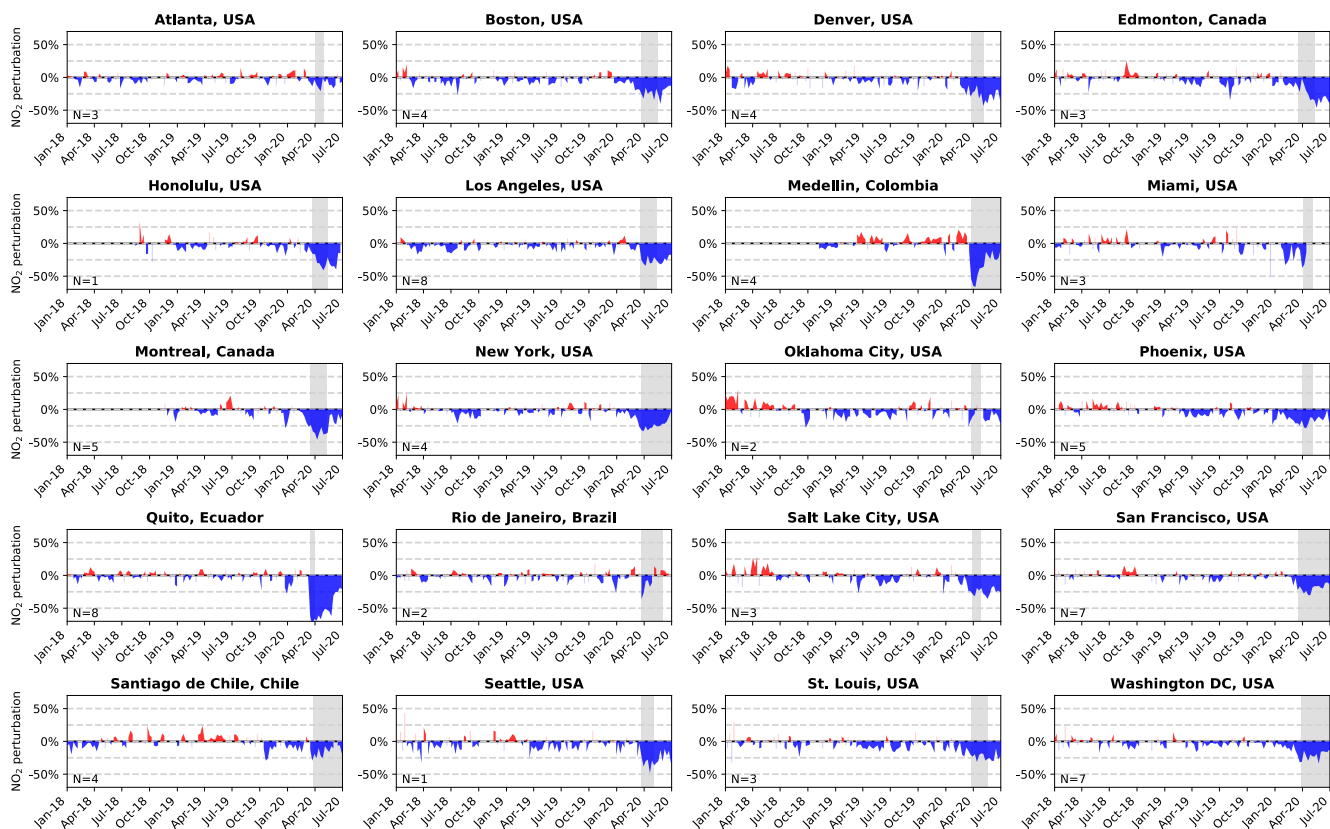
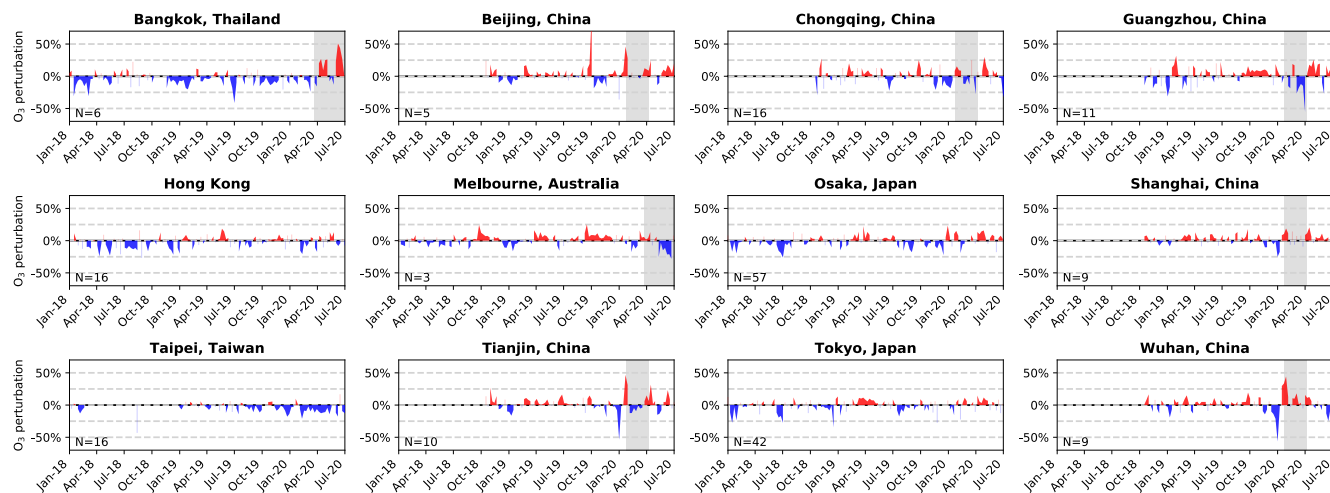
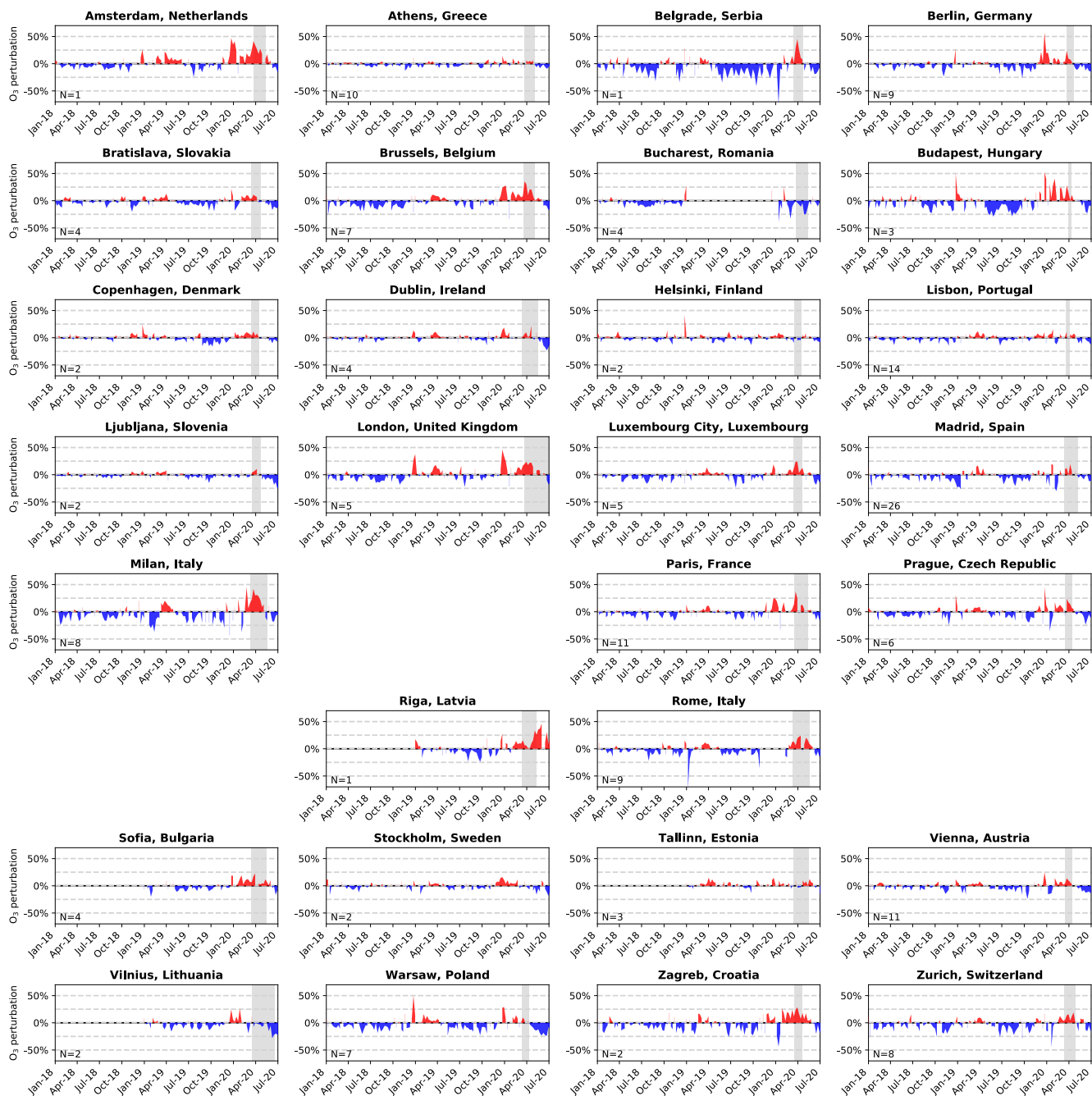


Figure A8: As Figure A6 but for North and South America.



575 Figure A9: Normalized fractional O₃ perturbations (observation - bias-corrected model, normalized by the bias-corrected model prediction) from Jan 1, 2018 through June 2020 for selected cities in Asia and Australia. Grey shaded areas indicate COVID-19 lockdown periods. Number of sites per city are shown in the bottom left of each panel.



580 **Figure A10:** As Figure A9 but for Europe. No observations are available for Reykjavik, Oslo, and Skopje.

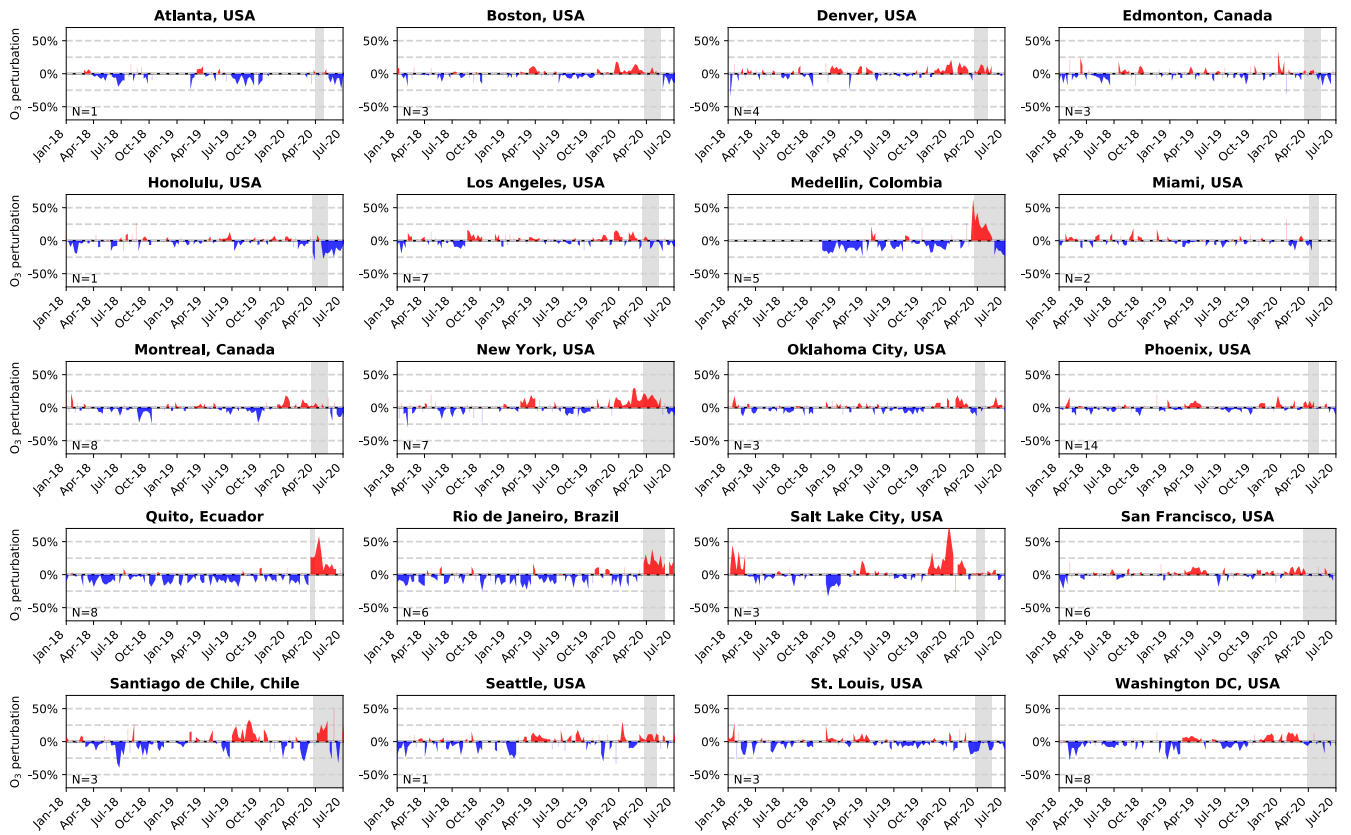
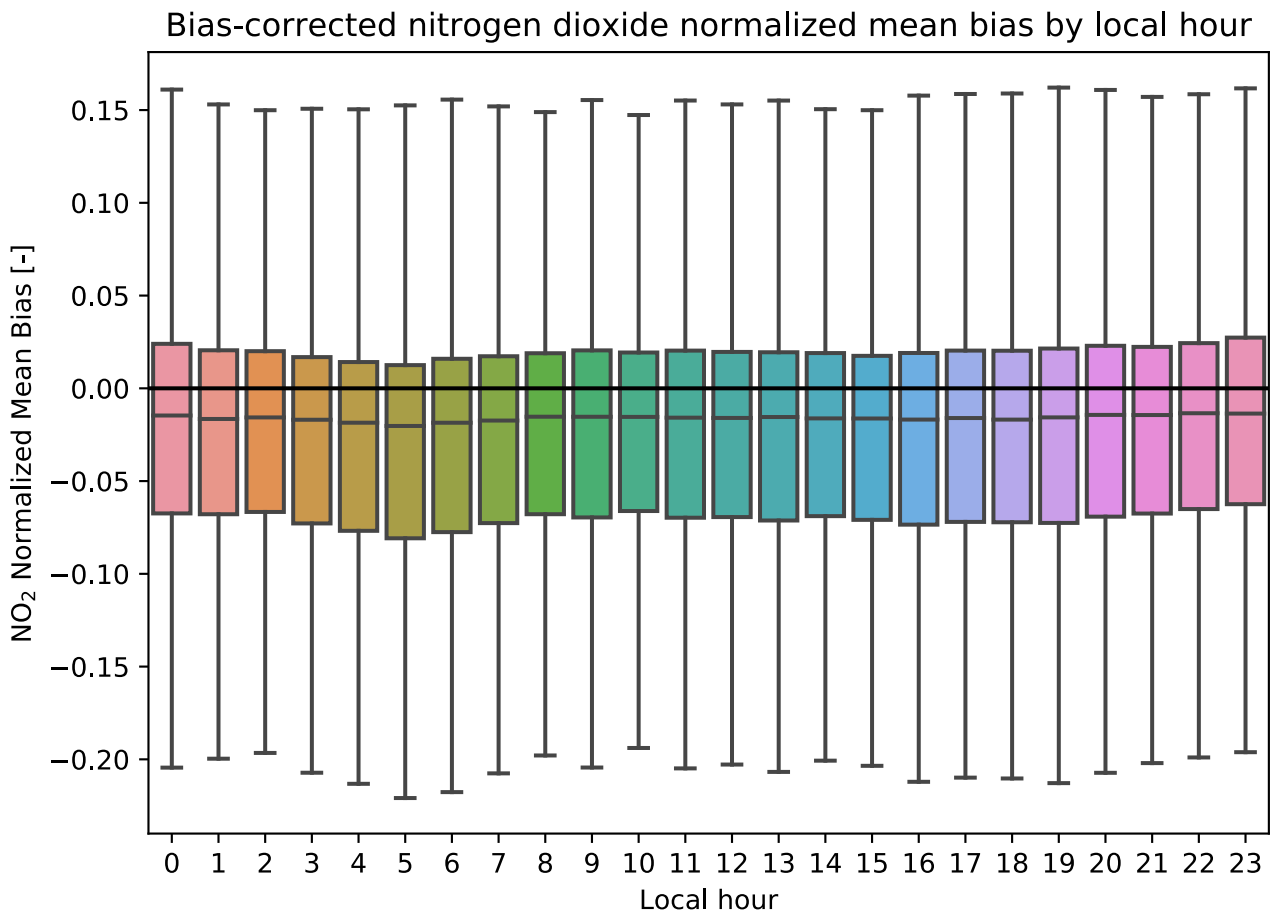


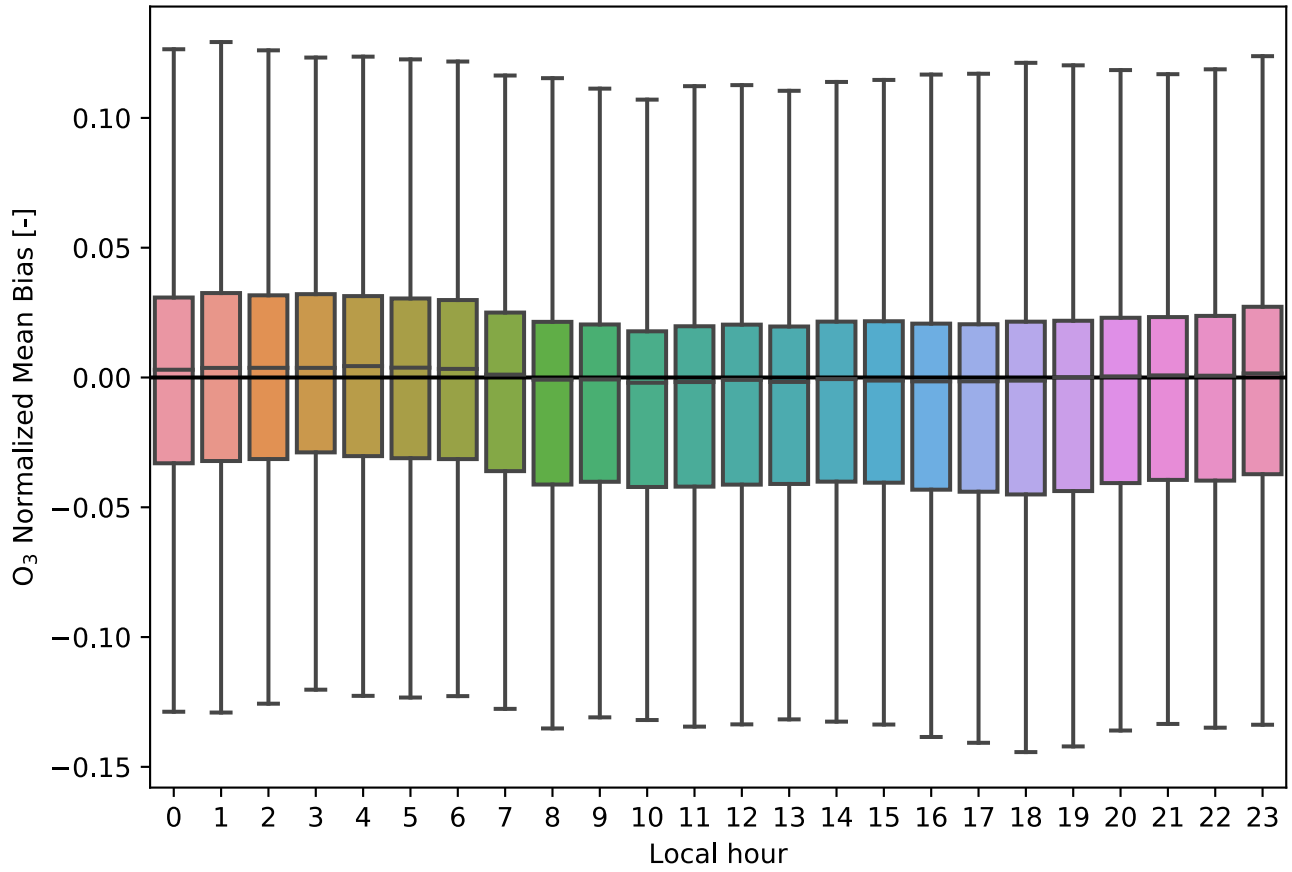
Figure A11: As Figure A9 but for North and South America.



585

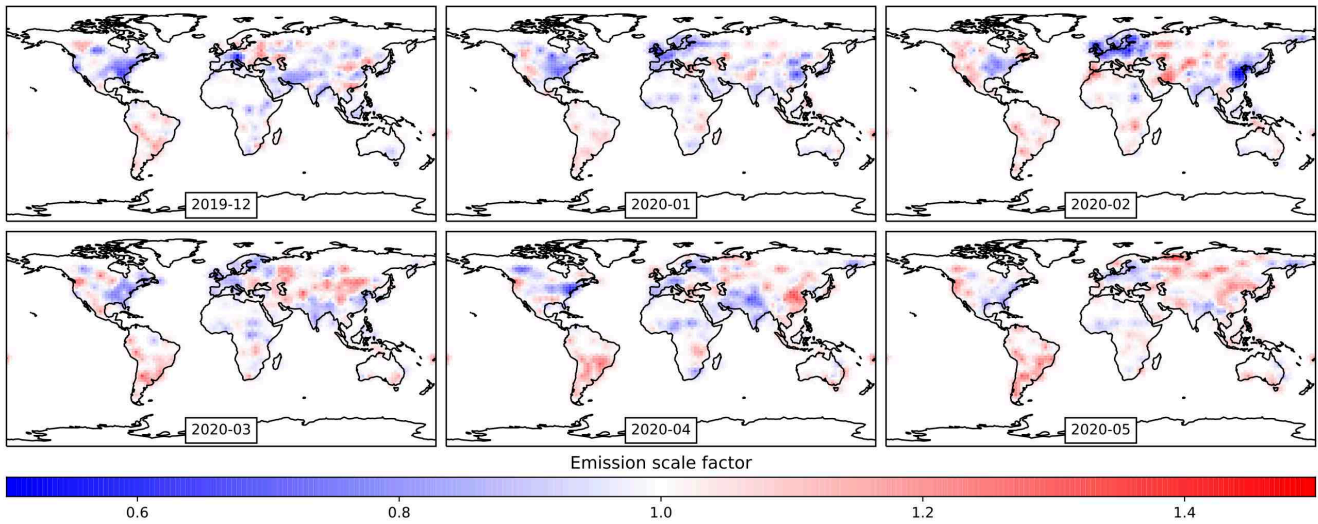
Figure A12: Distribution of normalized mean bias of the machine-learning corrected nitrogen dioxide concentrations at all available observation sites as a function of local hour. Shown are the results for the test dataset.

Bias-corrected ozone normalized mean bias by local hour



590 **Figure A13:** As Figure A12 but for ozone.

Emission scale factors based on OMI NO₂ observations



595 **Figure A14:** Emission scale factors used for model sensitivity simulation. Shown are the monthly average perturbations applied to the GEOS-CF anthropogenic base emissions.

Table A1: List of input features fed into the XGBoost machine learning model.

Short name	Description	Unit
no2	nitrogen dioxide	ppbv
no	nitrogen oxide	ppbv
noy	reactive nitrogen (no + no2 + nitrates)	ppbv
o3	ozone	ppbv
co	carbon monoxide	ppbv
acet	acetone	ppbv
alk4	alkanes	ppbv
ald2	acetaldehyde	ppbv
hcho	formaldehyde	ppbv
c2h6	ethane	ppbv
c3h8	propane	ppbv
bcpi	hydrophilic black carbon	ppbv
bcpo	hydrophobic black carbon	ppbv
ocpi	hydrophilic organic carbon	ppbv
ocpo	hydrophobic organic carbon	ppbv
eoh	ethanol	ppbv
dst1	dust with diameter of 0.7 microns	ppbv
dst2	dust with diameter of 1.4 microns	ppbv
dst3	dust with diameter of 2.4 microns	ppbv
dst4	dust with diameter of 4.5 microns	ppbv
h2o2	hydrogen peroxide	ppbv
hno3	nitric acid	ppbv
hno4	peroxynitric acid	ppbv
isop	isoprene	ppbv
macr	methacrolein	ppbv
mek	methyl ethyl ketone	ppbv
mvk	methyl vinyl ketone	ppbv
n2o5	dinitrogen pentoxide	ppbv
nh3	ammonia	ppbv
nh4	ammonium	ppbv
nit	inorganic nitrates	ppbv
pan	peroxyacetyl nitrate	ppbv
prpe	alkenes	ppbv
rcho	aldehyde	ppbv
sala	fine sea salt aerosol	ppbv
salc	coarse sea salt aerosol	ppbv
so2	sulfur dioxide	ppbv
soap	secondary organic aerosol precursor	ppbv
soas	simple secondary organic aerosol	ppbv
tolu	toluene	ppbv
xyle	xylene	ppbv
ox	odd oxygen (o3 + no2)	ppbv
pm25_gcc	total PM2.5	µg m-3
pm25ni_gcc	nitrate PM2.5	µg m-3
pm25su_gcc	sulfate PM2.5	µg m-3
pm25ss_gcc	sea salt PM2.5	µg m-3
pm25du_gcc	dust PM2.5	µg m-3
pm25bc_gcc	black carbon PM2.5	µg m-3
pm25oc_gcc	organic carbon PM2.5	µg m-3
pm25soa_gcc	secondary organic aerosol PM2.5	µg m-3
pm25_gocart	total PM2.5 as calculated by the GOCART model	µg m-3

600 **Table A1:** cont.

Short name	Description	unit
Hour	hour of day	-
Weekday	day of the week	-
Month	month of the year	-
Trendday	days since Jan 1, 2018	days
cldt	total cloud fraction	unitless
ps	surface pressure	Pa
q10m	specific humidity at 10m	kg/kg
t10m	temperature at 10m	K
tprec	total precipitation	mm
ts	skin surface temperature	K
u10m	10m East-West wind-speed	m/s
v10m	10m North-South wind speed	m/s
zpbl	planetary boundary layer height	m
emis_no	nitrogen oxide emissions	$\mu\text{g m}^{-2} \text{s}^{-1}$
emis_co	carbon monoxide emissions	$\mu\text{g m}^{-2} \text{s}^{-1}$
emis_acet	acetone emissions	$\mu\text{g m}^{-2} \text{s}^{-1}$
emis_ald2	acetaldehyde emissions	$\mu\text{g m}^{-2} \text{s}^{-1}$
emis_alk4	alkanes emissions	$\mu\text{g m}^{-2} \text{s}^{-1}$
emis_benz	benzene emissions	$\mu\text{g m}^{-2} \text{s}^{-1}$
emis_c2h6	ethane emissions	$\mu\text{g m}^{-2} \text{s}^{-1}$
emis_prpe	alkenes emissions	$\mu\text{g m}^{-2} \text{s}^{-1}$
emis_tolu	toluene emissions	$\mu\text{g m}^{-2} \text{s}^{-1}$
emis_xyle	xylene emissions	$\mu\text{g m}^{-2} \text{s}^{-1}$
emis_isop	isoprene emissions	$\mu\text{g m}^{-2} \text{s}^{-1}$
emis_bcpi	hydrophilic black carbon emissions	$\mu\text{g m}^{-2} \text{s}^{-1}$
emis_bcpo	hydrophobic black carbon emissions	$\mu\text{g m}^{-2} \text{s}^{-1}$
emis_ocpi	hydrophilic organic carbon emissions	$\mu\text{g m}^{-2} \text{s}^{-1}$
emis_ocpo	hydrophobic organic carbon emissions	$\mu\text{g m}^{-2} \text{s}^{-1}$
emis_sala	fine sea salt aerosol emissions	$\mu\text{g m}^{-2} \text{s}^{-1}$
emis_salc	coarse sea salt aerosol emissions	$\mu\text{g m}^{-2} \text{s}^{-1}$
emis_so2	sulfur dioxide emissions	$\mu\text{g m}^{-2} \text{s}^{-1}$
emis_soap	secondary organic aerosol precursor emissions	$\mu\text{g m}^{-2} \text{s}^{-1}$
emis_soas	simple secondary organic aerosol emissions	$\mu\text{g m}^{-2} \text{s}^{-1}$
emis_chbr3	bromoform emissions	$\mu\text{g m}^{-2} \text{s}^{-1}$

Table A2: National lockdown dates used for visualizations.

Country	Start Date	End Date
Australia	March 23	-
Austria	March 16	April 13
Belgium	March 18	April 4
Bosnia and Herzegovina	March 10	April 27
Brazil	March 13	June 2
Bulgaria	March 13	May 13
Canada	March 18	May 11
Chile	March 26	-
China	Jan 23	April 8
Colombia	March 24	June 1
Croatia	March 18	April 19
Czech Republic	March 16	April 12
Denmark	March 13	April 13
Ecuador	March 16	March 31
Estonia	March 13	May 15
Finland	March 16	April 15
France	March 17	May 11
Germany	March 23	April 20
Greece	March 23	May 4
Hungary	March 28	April 10
Iceland	March 21	May 4
India	March 25	-
Ireland	March 12	May 18
Italy	March 9	May 18
Latvia	March 13	May 12
Lithuania	March 16	June 18
Luxembourg	March 15	April 20
Macedonia	March 22	April 12
Malta	March 12	May 4
The Netherlands	March 23	May 11
Norway	March 12	May 11
Poland	March 13	April 11
Portugal	March 19	April 2
Romania	March 25	May 12
Serbia	March 15	April 21
Slovakia	March 16	April 22
Slovenia	March 16	April 20
Spain	March 14	May 9
Switzerland	March 13	April 27
Thailand	March 25	-
United Kingdom	March 23	-
United States	March 19	April 13

Table A3: Monthly changes in NO₂ concentrations relative to the bias-corrected model predictions for cities in Asia & Australia. Values in *italic* denote values that are statistically different from business-as-usual ($p < 0.001$ based on Kolmogorov-Smirnov test).

Location	#	Jan-20	Feb-20	Mar-20	Apr-20	May-20	Jun-20
Bangkok, Thailand	7	-7.8% (-10.9%-4.6%)	-11.5% (-15.3% <i>-7.7%</i>)	-20.4% (-25.9% <i>-14.9%</i>)	-27.4% (-31.8% <i>-23.0%</i>)	-39.1% (-43.6% <i>-34.5%</i>)	-25.7% (-30.7% <i>-20.7%</i>)
Beijing, China	5	-21.1% (-23.3% <i>-19.1%</i>)	-38.8% (-41.2% <i>-36.3%</i>)	-31.7% (-34.6% <i>-28.7%</i>)	-25.0% (-28.7% <i>-21.4%</i>)	-23.8% (-27.5% <i>-20.2%</i>)	-20.4% (-24.1% <i>-16.6%</i>)
Chongqing, China	16	-11.1% (-13.0% <i>-9.2%</i>)	-38.4% (-40.5% <i>-36.3%</i>)	-11.6% (-13.6% <i>-9.5%</i>)	-0.1% (-2.1% <i>1.9%</i>)	4.3% (2.0% <i>-6.5%</i>)	3.5% (1.1% <i>-6.0%</i>)
Guangzhou, China	11	-16.6% (-19.5% <i>-13.7%</i>)	-31.8% (-35.1% <i>-28.4%</i>)	-13.6% (-16.7% <i>-10.5%</i>)	-5.6% (-8.7% <i>-2.5%</i>)	-11.5% (-15.6% <i>-7.5%</i>)	-5.8% (-11.1% <i>-0.6%</i>)
Hong Kong	16	-6.9% (-8.8% <i>-4.9%</i>)	-13.9% (-16.0% <i>-11.8%</i>)	-3.7% (-5.8% <i>1.6%</i>)	-4.1% (-6.1% <i>-2.1%</i>)	-4.7% (-6.9% <i>-2.4%</i>)	-12.8% (-15.7% <i>-10.0%</i>)
Melbourne, Australia	2	4.6% (-5.6% <i>-14.8%</i>)	1.5% (-9.1% <i>-12.1%</i>)	-7.6% (-16.5% <i>-1.4%</i>)	-13.9% (-21.9% <i>-5.8%</i>)	-11.9% (-19.3% <i>-4.9%</i>)	-7.8% (-14.1% <i>-1.6%</i>)
Osaka, Japan	90	-14.4% (-15.4% <i>-13.4%</i>)	-6.4% (-7.3% <i>-5.5%</i>)	-13.4% (-14.3% <i>-12.5%</i>)	-25.7% (-26.8% <i>-24.7%</i>)	-28.1% (-29.2% <i>-27.0%</i>)	-17.4% (-18.6% <i>-16.3%</i>)
Shanghai, China	9	-14.4% (-16.5% <i>-12.3%</i>)	-39.8% (-42.1% <i>-37.5%</i>)	-23.3% (-25.7% <i>-20.8%</i>)	-19.3% (-21.7% <i>-17.0%</i>)	-5.5% (-8.4% <i>-2.7%</i>)	-1.9% (-5.0% <i>1.2%</i>)
Taipei, Taiwan	18	-7.8% (-9.4% <i>-6.2%</i>)	-6.4% (-8.0% <i>-4.8%</i>)	-5.1% (-6.7% <i>-3.6%</i>)	-2.0% (-3.6% <i>0.3%</i>)	-3.0% (-4.7% <i>-1.2%</i>)	-11.1% (-13.0% <i>-9.3%</i>)
Tianjin, China	10	-7.2% (-8.7% <i>-5.8%</i>)	-32.1% (-34.0% <i>-30.3%</i>)	-14.5% (-16.5% <i>-12.4%</i>)	-8.4% (-10.9% <i>-5.9%</i>)	-1.0% (-3.7% <i>1.7%</i>)	-2.5% (-5.5% <i>0.6%</i>)
Tokyo, Japan	79	1.6% (0.5% <i>-2.7%</i>)	-2.5% (-3.6% <i>-1.4%</i>)	-13.9% (-15.1% <i>-12.8%</i>)	-21.3% (-22.5% <i>-20.1%</i>)	-26.7% (-28.0% <i>-25.5%</i>)	-12.0% (-13.3% <i>-10.6%</i>)
Wuhan, China	9	-20.4% (-23.6% <i>-17.3%</i>)	-56.3% (-59.4% <i>-53.2%</i>)	-51.4% (-54.6% <i>-48.2%</i>)	-22.0% (-25.3% <i>-18.7%</i>)	-15.0% (-18.7% <i>-11.2%</i>)	-11.1% (-15.9% <i>-6.2%</i>)

Table A4: Monthly changes in NO₂ concentrations relative to the bias-corrected model predictions for cities in Europe. Values in *italic* denote values that are statistically different from business-as-usual ($p < 0.001$ based on Kolmogorov-Smirnov test).

Location	#	Jan-20	Feb-20	Mar-20	Apr-20	May-20	Jun-20
Amsterdam, Netherlands	1	-1.5% (-8.2%-5.3%)	-8.5% (-17.4%-0.4%)	-16.2% (-25.7% <i>-6.4%</i>)	-27.2% (-36.8% <i>-17.6%</i>)	-18.4% (-29.9% <i>-6.9%</i>)	-17.2% (-28.2% <i>-6.3%</i>)
Athens, Greece	11	<i>13.8%</i> (11.4%-16.1%)	1.9% (-0.2%-4.1%)	-5.0% (-7.1% <i>-3.0%</i>)	-26.4% (-28.7% <i>-24.2%</i>)	-8.8% (-10.9% <i>-6.7%</i>)	-12.7% (-15.0% <i>-10.5%</i>)
Belgrade, Serbia	1	2.8% (-5.1%-10.7%)	-10.6% (-19.8% <i>-1.4%</i>)	-40.9% (-50.2% <i>-31.6%</i>)	-71.7% (-81.4% <i>-62.0%</i>)	-31.0% (-44.1% <i>-17.8%</i>)	-17.0% (-33.4% <i>-0.6%</i>)
Berlin, Germany	18	2.1% (0.4%-3.8%)	-7.3% (-9.4% <i>-5.2%</i>)	-9.7% (-11.6% <i>-7.8%</i>)	-25.3% (-27.3% <i>-23.3%</i>)	-12.6% (-15.0% <i>-10.2%</i>)	-15.4% (-17.9% <i>-12.9%</i>)
Bratislava, Slovakia	5	0.3% (-2.8%-3.3%)	-15.7% (-19.8% <i>-11.5%</i>)	-18.3% (-22.4% <i>-14.3%</i>)	-18.2% (-22.3% <i>-14.2%</i>)	-12.4% (-17.6% <i>-7.1%</i>)	-14.9% (-20.5% <i>-9.3%</i>)
Brussels, Belgium	17	-5.2% (-7.1% <i>-3.4%</i>)	-11.8% (-14.2% <i>-9.3%</i>)	-25.4% (-27.4% <i>-23.4%</i>)	-40.8% (-42.6% <i>-39.0%</i>)	-30.7% (-33.0% <i>-28.5%</i>)	-19.7% (-22.3% <i>-17.0%</i>)
Bucharest, Romania	8	-1.7% (-4.5%-1.0%)	-9.9% (-12.9% <i>-7.0%</i>)	-21.6% (-24.6% <i>-18.6%</i>)	-39.8% (-43.0% <i>-36.5%</i>)	-23.3% (-26.9% <i>-19.8%</i>)	-23.0% (-26.5% <i>-19.5%</i>)
Budapest, Hungary	5	-2.2% (-5.3%-0.8%)	-9.2% (-12.8% <i>-5.5%</i>)	-12.0% (-15.5% <i>-8.6%</i>)	-23.6% (-27.2% <i>-20.0%</i>)	-24.4% (-28.8% <i>-20.0%</i>)	-25.7% (-30.2% <i>-21.3%</i>)
Copenhagen, Denmark	4	-1.7% (-6.4%-2.9%)	-9.6% (-14.9% <i>-4.3%</i>)	-19.0% (-23.4% <i>-14.7%</i>)	-25.7% (-30.1% <i>-21.4%</i>)	-18.7% (-24.1% <i>-13.3%</i>)	-13.8% (-18.4% <i>-9.1%</i>)
Dublin, Ireland	5	-8.7% (-14.7% <i>-2.7%</i>)	-9.3% (-17.2% <i>-1.5%</i>)	-28.8% (-34.4% <i>-23.1%</i>)	-39.2% (-43.7% <i>-34.8%</i>)	-38.0% (-44.2% <i>-31.8%</i>)	-40.8% (-47.3% <i>-34.2%</i>)
Helsinki, Finland	6	-9.1% (-13.2% <i>-4.9%</i>)	-15.2% (-19.2% <i>-11.1%</i>)	-18.2% (-22.0% <i>-14.5%</i>)	-38.8% (-43.0% <i>-34.5%</i>)	-33.0% (-37.5% <i>-28.6%</i>)	-25.9% (-29.7% <i>-22.2%</i>)
Lisbon, Portugal	20	-6.1% (-8.1% <i>-4.1%</i>)	-3.4% (-5.3% <i>-1.5%</i>)	-26.9% (-29.4% <i>-24.3%</i>)	-41.3% (-44.1% <i>-38.6%</i>)	-32.5% (-35.4% <i>-29.6%</i>)	-28.1% (-32.0% <i>-24.1%</i>)
Ljubljana, Slovenia	1	-3.8% (-11.6%-4.1%)	-26.0% (-33.7% <i>-18.4%</i>)	-47.9% (-56.2% <i>-39.5%</i>)	-49.8% (-59.1% <i>-40.2%</i>)	-41.4% (-53.1% <i>-29.7%</i>)	-42.6% (-54.2% <i>-31.0%</i>)
London, United Kingdom	11	-3.6% (-6.0% <i>-1.1%</i>)	-4.3% (-7.3% <i>-1.2%</i>)	-17.0% (-19.7% <i>-14.3%</i>)	-35.9% (-38.1% <i>-33.6%</i>)	-35.1% (-37.8% <i>-32.3%</i>)	-28.8% (-31.9% <i>-25.8%</i>)
Luxembourg City, Luxembourg	9	3.7% (1.0%-6.4%)	-3.4% (-6.7% <i>-0.1%</i>)	-24.4% (-27.4% <i>-21.4%</i>)	-40.2% (-42.9% <i>-37.6%</i>)	-27.0% (-30.1% <i>-23.9%</i>)	-19.2% (-22.7% <i>-15.7%</i>)
Madrid, Spain	37	0.9% (-0.5%-2.4%)	-9.4% (-10.8% <i>-8.0%</i>)	-31.7% (-33.6% <i>-29.8%</i>)	-60.6% (-62.6% <i>-58.6%</i>)	-51.8% (-54.0% <i>-49.6%</i>)	-40.4% (-42.8% <i>-38.0%</i>)
Milan, Italy	19	<i>10.0%</i> (8.8%-11.2%)	-2.0% (-3.6% <i>-0.3%</i>)	-25.7% (-27.2% <i>-24.2%</i>)	-41.6% (-43.3% <i>-39.9%</i>)	-34.7% (-36.9% <i>-32.6%</i>)	-24.4% (-26.6% <i>-22.1%</i>)
Oslo, Norway	12	-6.9% (-9.3% <i>-4.5%</i>)	-16.0% (-18.5% <i>-13.5%</i>)	-25.4% (-28.1% <i>-22.6%</i>)	-26.3% (-29.4% <i>-23.2%</i>)	-18.8% (-22.4% <i>-15.2%</i>)	-12.2% (-15.7% <i>-8.7%</i>)
Paris, France	28	-3.2% (-4.5% <i>-1.8%</i>)	-12.7% (-14.4% <i>-11.0%</i>)	-28.0% (-29.5% <i>-26.6%</i>)	-46.6% (-48.0% <i>-45.2%</i>)	-35.7% (-37.3% <i>-34.1%</i>)	-21.1% (-22.9% <i>-19.3%</i>)
Prague, Czech Republic	9	3.9% (1.6%-6.2%)	-9.1% (-12.1% <i>-6.0%</i>)	-10.1% (-12.6% <i>-7.5%</i>)	-16.6% (-19.0% <i>-14.2%</i>)	-16.7% (-19.5% <i>-13.9%</i>)	-17.7% (-20.6% <i>-14.8%</i>)
Reykjavik, Iceland	3	-20.9% (-28.3% <i>-13.5%</i>)	-17.4% (-23.8% <i>-10.9%</i>)	-20.0% (-27.4% <i>-12.6%</i>)	-28.1% (-36.3% <i>-19.9%</i>)	-6.7% (-17.5% <i>-3.0%</i>)	-0.2% (-9.9% <i>-9.4%</i>)
Riga, Latvia	1	-5.7% (-17.6%-6.3%)	-7.6% (-20.5%-5.3%)	-23.9% (-35.1% <i>-12.7%</i>)	-45.5% (-60.5% <i>-30.6%</i>)	-48.9% (-62.8% <i>-35.0%</i>)	-12.6% (-25.0% <i>-0.2%</i>)
Rome, Italy	15	N/A	-0.9% (-3.3%-1.5%)	-32.3% (-34.3% <i>-30.2%</i>)	-50.0% (-52.1% <i>-47.8%</i>)	-39.3% (-41.6% <i>-36.9%</i>)	-24.2% (-26.8% <i>-21.7%</i>)
Skopje, Macedonia	1	-9.5% (-17.5% <i>-2.5%</i>)	5.6% (-2.9%-14.3%)	-8.1% (-16.6%-0.3%)	-35.5% (-43.9% <i>-27.2%</i>)	-32.2% (-41.7% <i>-22.7%</i>)	-18.0% (-27.8% <i>-8.2%</i>)
Sofia, Bulgaria	4	8.5% (3.8%-	-3.4% (-8.4%-	-16.5% (-	-27.3% (-	-20.3% (-	-10.7% (-

		13.2%)	1.6%)	21.8%--11.2%)	34.7%--19.9%)	29.4%--11.1%)	18.4%--3.5%)
Stockholm, Sweden	6	-11.1% (- 15.4%--6.8%)	-11.8% (- 15.8%--7.8%)	-18.0% (- 22.0%--14.1%)	-33.0% (- 37.1%--28.9%)	-23.7% (- 28.0%--19.4%)	-20.9% (- 25.5%--16.4%)
Tallinn, Estonia	3	-3.2% (-12.0%- 5.6%)	-12.3% (- 21.3%--3.3%)	-14.8% (- 24.1%--5.4%)	-25.2% (- 34.3%--16.0%)	-22.3% (- 31.4%--13.5%)	-9.7% (-17.3%- -2.1%)
Vienna, Austria	28	-2.3% (-3.6%-- 0.9%)	-14.4% (- 16.3%--12.6%)	-20.6% (- 22.3%--18.9%)	-26.2% (- 27.9%--24.5%)	-16.5% (- 18.8%--14.2%)	-25.4% (- 27.6%--23.1%)
Vilnius, Lithuania	4	-11.8% (- 16.7%--7.0%)	-3.5% (-8.7%- 1.7%)	-10.1% (- 15.0%--5.2%)	-24.4% (- 29.8%--18.9%)	-16.2% (- 22.2%--10.2%)	-20.3% (- 26.9%--13.7%)
Warsaw, Poland	7	-10.4% (- 13.1%--7.6%)	-15.7% (- 18.7%--12.6%)	-15.2% (- 18.0%--12.4%)	-26.0% (- 28.9%--23.1%)	-18.3% (- 21.6%--15.1%)	-17.5% (- 21.4%--13.6%)
Zagreb, Croatia	3	8.0% (2.6%- 13.4%)	-15.2% (- 21.1%--9.4%)	-32.0% (- 38.0%--25.9%)	-51.5% (- 57.7%--45.2%)	-50.0% (- 56.7%--43.3%)	-42.3% (- 50.2%--34.4%)
Zurich, Switzerland	8	2.2% (0.0%- 4.5%)	-11.8% (- 14.9%--8.6%)	-15.1% (- 17.9%--12.3%)	-28.0% (- 30.9%--25.2%)	-23.4% (- 27.0%--19.8%)	-25.5% (- 29.1%--22.0%)

610

Table A5: Monthly changes in NO₂ concentrations relative to the bias-corrected model predictions for cities in North and South America. Values in *italic* denote values that are statistically different from business-as-usual ($p < 0.001$ based on Kolmogorov-Smirnov test).

Location	#	Jan-20	Feb-20	Mar-20	Apr-20	May-20	Jun-20
Atlanta, USA	3	9.7% (4.6%-14.9%)	0.8% (-4.5%-6.2%)	-3.3% (-8.7%-2.2%)	-12.4% (-17.9%-6.9%)	-6.7% (-12.5%-1.2%)	-7.1% (-13.5%-1.1%)
Boston, USA	4	-8.4% (-12.5%-4.8%)	-5.1% (-9.2%-1.4%)	-20.7% (-25.8%-15.7%)	-23.4% (-29.3%-17.4%)	-27.0% (-33.4%-20.6%)	-14.7% (-20.6%-8.4%)
Denver, USA	4	-4.5% (-7.5%-1.9%)	-7.5% (-11.1%-4.3%)	-20.5% (-24.6%-16.5%)	-21.2% (-26.1%-16.3%)	-35.8% (-41.3%-30.4%)	-24.1% (-29.5%-18.7%)
Edmonton, Canada	3	-4.0% (-7.5%-0.7%)	-11.5% (-15.3%-7.6%)	-15.2% (-20.1%-10.3%)	-18.0% (-24.5%-11.4%)	-34.9% (-43.5%-26.3%)	-32.3% (-41.1%-23.5%)
Honolulu, USA	1	-3.1% (-16.1%-10.0%)	-0.9% (-15.6%-13.9%)	-11.7% (-26.2%-2.8%)	-28.3% (-42.2%-14.3%)	-30.6% (-47.0%-14.3%)	-26.7% (-42.7%-10.6%)
Los Angeles, USA	8	4.7% (2.8%-6.9%)	-4.1% (-6.3%-1.9%)	-11.9% (-15.1%-8.7%)	-28.2% (-31.7%-24.8%)	-27.5% (-31.2%-24.2%)	-23.4% (-27.6%-19.3%)
Medellin, Colombia	4	-2.0% (-6.6%-2.6%)	11.6% (7.1%-16.0%)	-7.1% (-12.1%-2.6%)	-51.9% (-56.3%-47.8%)	-24.8% (-29.5%-20.1%)	-21.1% (-26.2%-16.1%)
Miami, USA	3	-4.1% (-14.5%-6.3%)	-22.6% (-32.8%-12.4%)	-12.9% (-21.7%-4.2%)	-29.2% (-40.9%-17.4%)	N/A	N/A
Montreal, Canada	5	-5.4% (-8.9%-2.1%)	-4.4% (-8.3%-0.8%)	-22.9% (-27.4%-18.7%)	-36.4% (-42.5%-30.7%)	-25.8% (-32.5%-19.1%)	-14.7% (-21.3%-8.1%)
New York, USA	4	-5.5% (-9.1%-2.4%)	-8.0% (-11.4%-4.8%)	-20.8% (-24.6%-17.0%)	-29.7% (-34.2%-25.2%)	-25.1% (-30.4%-19.8%)	-17.1% (-23.5%-10.7%)
Oklahoma City, USA	2	-0.9% (-6.9%-45.0%)	-3.5% (-10.4%-3.4%)	-7.1% (-13.6%-1.3%)	-2.8% (-9.5%-3.8%)	-13.9% (-20.3%-7.4%)	-8.0% (-13.9%-2.2%)
Phoenix, USA	5	-9.5% (-12.0%-7.2%)	-12.6% (-15.7%-9.5%)	-19.8% (-23.6%-16.0%)	-22.2% (-26.3%-18.1%)	-13.8% (-18.1%-9.5%)	-11.0% (-16.1%-6.0%)
Quito, Ecuador	8	-10.7% (-13.9%-7.6%)	2.5% (-0.5%-5.4%)	-34.7% (-37.5%-31.8%)	-64.3% (-67.2%-61.4%)	-55.8% (-58.8%-52.7%)	-24.9% (-27.9%-21.8%)
Rio de Janeiro, Brazil	2	-4.9% (-11.5%-1.7%)	0.8% (-5.7%-7.2%)	-5.2% (-11.9%-1.5%)	-15.9% (-22.6%-9.2%)	6.5% (1.5%-12.2%)	4.4% (-0.5%-9.4%)
Salt Lake City, USA	3	-1.4% (-5.0%-2.2%)	-5.5% (-9.8%-1.9%)	-15.4% (-21.2%-9.8%)	-24.7% (-31.9%-17.4%)	-28.3% (-36.5%-20.0%)	-20.6% (-29.6%-11.6%)
San Francisco, USA	7	4.6% (2.1%-7.2%)	-1.8% (-4.4%-0.7%)	-14.8% (-18.1%-11.5%)	-26.7% (-30.8%-22.6%)	-18.4% (-22.7%-14.0%)	-15.7% (-20.6%-10.8%)
Santiago de Chile, Chile	4	-6.6% (-16.9%-3.6%)	-10.5% (-19.2%-1.8%)	-8.4% (-16.4%-1.1%)	-20.9% (-26.8%-14.9%)	-11.8% (-16.7%-7.0%)	-6.9% (-11.9%-1.8%)
Seattle, USA	1	-8.6% (-18.0%-0.9%)	-2.5% (-11.7%-6.7%)	-12.7% (-22.4%-2.9%)	-34.0% (-44.7%-23.2%)	-28.9% (-41.6%-16.7%)	-19.8% (-33.6%-6.1%)
St. Louis, USA	3	-4.4% (-9.4%-0.6%)	-11.9% (-17.3%-6.6%)	-16.4% (-21.7%-11.1%)	-24.8% (-31.1%-18.6%)	-23.9% (-30.4%-17.4%)	-23.8% (-30.0%-17.6%)
Washington DC, USA	7	-7.0% (-9.9%-4.0%)	-10.0% (-13.1%-6.9%)	-18.4% (-21.9%-14.8%)	-22.3% (-26.4%-18.2%)	-25.2% (-30.0%-20.3%)	-14.6% (-19.4%-9.9%)

Table A6: Monthly changes in O₃ concentrations relative to the bias-corrected model predictions for cities in Asia & Australia. Values in *italic* denote values that are statistically different from business-as-usual (p<0.001 based on Kolmogorov-Smirnov test).

Location	#	20-Jan	20-Feb	20-Mar	20-Apr	20-May	20-Jun
Bangkok, Thailand	6	-6.1% (-9.4% - 2.8%)	-2.8% (-6.1% - 0.5%)	-10.2% (-13.9% - -6.5%)	<i>11.2%</i> (7.4% - 15.1%)	3.6% (-2.1% - 9.2%)	<i>34.7%</i> (28.0% - 41.3%)
Beijing, China	5	10.9% (6.2% - 15.6%)	1.4% (-2.2% - 4.9%)	1.7% (-1.1% - 4.5%)	<i>11.7%</i> (9.4% - 14.0%)	-4.4% (-6.1% - -2.3%)	9.5% (8.1% - 11.0%)
Chongqing, China	16	-3.6% (-7.0% - 0.3%)	-2.4% (-4.9% - 0.1%)	4.3% (2.6% - 5.9%)	3.1% (1.6% - 4.6%)	6.9% (5.8% - 8.1%)	2.1% (0.8% - 3.3%)
Guangzhou, China	11	-0.9% (-3.4% - 1.7%)	5.0% (2.3% - 7.8%)	-15.4% (-18.0% - -12.9%)	4.8% (2.6% - 7.0%)	11.3% (9.4% - 13.2%)	-1.5% (-3.8% - 0.9%)
Hong Kong	16	-0.1% (-2.7% - 2.6%)	-8.3% (-10.9% - -5.6%)	-2.9% (-5.6% - 0.2%)	-2.3% (-4.8% - 0.1%)	9.0% (5.0% - 12.9%)	-4.5% (-10.3% - 1.4%)
Melbourne, Australia	3	1.1% (-3.7% - 6.0%)	-8.9% (-14.4% - -3.4%)	3.7% (-1.6% - 8.9%)	2.7% (-2.5% - 7.9%)	-6.1% (-11.6% - -0.7%)	-19.6% (-25.1% - -14.1%)
Osaka, Japan	57	<i>12.7%</i> (11.3% - 14.2%)	-3.6% (-4.8% - -2.4%)	1.4% (0.4% - 2.3%)	<i>11.4%</i> (10.7% - 12.2%)	3.3% (2.5% - 4.0%)	1.2% (0.3% - 2.1%)
Shanghai, China	9	-2.9% (-5.2% - 0.5%)	5.8% (3.7% - 7.9%)	0.6% (-1.0% - 2.2%)	11.4% (9.9% - 12.9%)	2.1% (0.9% - 3.3%)	1.5% (-0.0% - 3.0%)
Taipei, Taiwan	16	-0.9% (-2.4% - 0.6%)	-9.9% (-11.3% - -8.6%)	-8.0% (-9.2% - -6.8%)	-9.6% (-10.6% - -8.6%)	-6.6% (-8.0% - -5.1%)	-5.2% (-7.1% - -3.3%)
Tianjin, China	10	5.9% (2.6% - 9.2%)	-8.1% (-10.5% - -5.8%)	-1.4% (-3.4% - 0.6%)	<i>14.1%</i> (12.4% - 15.8%)	-8.4% (-9.7% - -7.2%)	7.3% (6.1% - 8.5%)
Tokyo, Japan	42	-4.5% (-6.3% - -2.7%)	1.7% (0.2% - 3.3%)	0.3% (-0.9% - 1.4%)	6.4% (5.4% - 7.4%)	3.8% (2.8% - 4.8%)	-1.4% (-2.6% - 0.3%)
Wuhan, China	9	8.6% (4.7% - 12.4%)	12.3% (9.7% - 14.9%)	4.3% (2.3% - 6.3%)	10.4% (8.7% - 12.0%)	-2.4% (-3.7% - 1.1%)	-8.2% (-9.7% - -6.7%)

Table A7: Monthly changes in O₃ concentrations relative to the bias-corrected model predictions for cities in Europe. Values in *italic* denote values that are statistically different from business-as-usual ($p < 0.001$ based on Kolmogorov-Smirnov test).

Location	#	Jan-20	Feb-20	Mar-20	Apr-20	May-20	Jun-20
Amsterdam, Netherlands	1	21.6% (11.6% - 31.6%)	11.4% (5.9% - 16.9%)	22.5% (16.9% - 28.1%)	26.4% (21.1% - 31.6%)	7.1% (2.7% - 11.4%)	-3.7% (-8.1% - 0.7%)
Athens, Greece	10	1.0% (-1.3% - 3.2%)	4.3% (1.9% - 6.6%)	0.0% (-1.9% - 2.0%)	4.4% (2.6% - 6.1%)	-3.9% (-5.5% - 2.2%)	-5.7% (-7.3% - 4.0%)
Belgrade, Serbia	1	-25.2% (-39.7% - -10.8%)	0.9% (-7.3% - 9.1%)	15.2% (9.0% - 21.5%)	15.0% (10.1% - 19.9%)	-5.5% (-10.5% - -0.5%)	-14.3% (-19.8% - -8.8%)
Berlin, Germany	9	8.2% (5.4% - 11.1%)	7.3% (5.5% - 9.2%)	7.4% (5.7% - 9.1%)	1.8% (0.6% - 3.1%)	-6.2% (-7.4% - 4.9%)	-9.0% (-10.2% - -7.7%)
Bratislava, Slovakia	4	-7.1% (-11.1% - -3.1%)	8.1% (5.7% - 10.5%)	6.1% (4.1% - 8.2%)	1.3% (-0.3% - 2.9%)	-3.2% (-4.8% - 1.3%)	-11.2% (-12.9% - -9.3%)
Brussels, Belgium	7	8.7% (5.6% - 11.9%)	11.2% (9.2% - 13.3%)	16.7% (14.5% - 18.8%)	18.3% (16.5% - 20.1%)	2.9% (1.3% - 4.5%)	-5.9% (-7.4% - 4.3%)
Bucharest, Romania	4	-12.3% (-16.8% - -7.8%)	0.4% (-3.1% - 3.8%)	-11.8% (-14.4% - -9.2%)	-9.1% (-11.2% - -6.9%)	-13.3% (-15.5% - -11.2%)	-3.6% (-5.8% - 0.8%)
Budapest, Hungary	3	18.2% (8.6% - 27.2%)	20.1% (15.8% - 24.4%)	16.1% (12.4% - 19.8%)	4.4% (1.6% - 7.3%)	-2.7% (-5.4% - 0.0%)	-13.1% (-15.9% - -10.2%)
Copenhagen, Denmark	2	4.9% (2.1% - 7.7%)	5.1% (3.0% - 7.3%)	7.5% (5.7% - 9.4%)	1.8% (0.1% - 3.5%)	-2.4% (-4.0% - 0.5%)	-5.2% (-6.7% - 3.2%)
Dublin, Ireland	4	5.6% (2.3% - 8.8%)	-2.0% (-4.6% - 0.6%)	2.7% (-0.1% - 5.5%)	8.7% (5.6% - 11.5%)	-1.9% (-4.4% - 0.7%)	-13.8% (-16.7% - -10.9%)
Helsinki, Finland	2	5.5% (0.9% - 10.1%)	-0.3% (-4.4% - 3.9%)	-3.7% (-7.5% - 0.0%)	-2.2% (-5.5% - 1.1%)	3.1% (0.7% - 5.5%)	-4.7% (-7.1% - 1.7%)
Lisbon, Portugal	14	6.6% (4.8% - 8.3%)	-3.8% (-5.5% - -2.2%)	2.6% (1.5% - 3.7%)	4.8% (3.8% - 5.8%)	-6.4% (-7.4% - 5.5%)	-4.3% (-5.4% - 3.1%)
Ljubljana, Slovenia	2	-4.9% (-8.5% - 0.9%)	0.2% (-2.5% - 2.9%)	0.8% (-1.5% - 3.0%)	3.5% (1.7% - 5.3%)	-6.4% (-8.3% - 4.0%)	-12.4% (-14.4% - -10.4%)
London, United Kingdom	5	8.6% (4.4% - 12.8%)	5.6% (2.8% - 8.3%)	14.9% (12.5% - 17.2%)	20.3% (17.9% - 22.7%)	6.7% (4.6% - 8.9%)	-2.5% (-4.7% - 0.3%)
Luxembourg City, Luxembourg	5	0.8% (-2.5% - 4.2%)	3.4% (1.1% - 5.7%)	13.0% (10.9% - 15.2%)	10.2% (8.3% - 12.1%)	-0.2% (-2.0% - 1.5%)	-9.5% (-11.3% - -7.8%)
Madrid, Spain	26	0.7% (-1.3% - 2.7%)	-9.2% (-11.1% - -7.3%)	4.7% (3.7% - 5.7%)	6.4% (5.5% - 7.3%)	-2.2% (-3.0% - 1.5%)	-6.1% (-6.8% - 5.4%)
Milan, Italy	8	5.3% (-8.6% - 19.2%)	14.6% (7.9% - 21.3%)	22.6% (19.1% - 26.1%)	25.6% (23.3% - 27.9%)	0.7% (-1.1% - 2.6%)	-10.3% (-12.0% - -8.6%)
Paris, France	11	5.7% (2.9% - 8.5%)	3.8% (2.1% - 5.6%)	14.5% (12.8% - 16.3%)	8.3% (6.9% - 9.6%)	2.5% (1.2% - 3.7%)	-6.2% (-7.5% - 4.9%)
Prague, Czech Republic	6	-11.0% (-14.6% - -7.3%)	10.8% (8.5% - 13.0%)	9.3% (7.2% - 11.4%)	6.9% (5.2% - 8.6%)	-2.6% (-4.2% - 1.0%)	-12.6% (-14.2% - -11.1%)
Riga, Latvia	1	-1.3% (-6.1% - 3.5%)	8.1% (3.9% - 12.4%)	11.7% (7.9% - 15.5%)	3.7% (0.8% - 6.6%)	32.6% (28.2% - 37.1%)	20.6% (14.6% - 26.6%)
Rome, Italy	9	N/A	-5.1% (-8.4% - -1.7%)	8.2% (6.1% - 10.3%)	15.4% (13.4% - 17.3%)	12.5% (10.8% - 14.3%)	-5.8% (-7.4% - 4.3%)
Sofia, Bulgaria	4	3.7% (0.3% - 7.2%)	11.1% (8.4% - 13.8%)	10.6% (8.5% - 12.7%)	4.0% (1.8% - 6.1%)	4.7% (2.8% - 6.7%)	-3.8% (-5.6% - 1.8%)
Stockholm, Sweden	2	5.8% (2.5% - 9.0%)	5.8% (2.8% - 8.8%)	0.6% (-1.9% - 3.1%)	-3.6% (-5.7% - -1.5%)	-8.1% (-10.5% - -5.8%)	-2.2% (-4.4% - 0.1%)
Tallinn, Estonia	3	3.1% (-0.5% - 6.7%)	2.1% (-1.1% - 5.2%)	1.1% (-1.9% - 4.1%)	0.2% (-2.4% - 2.8%)	7.0% (4.1% - 10.0%)	-0.5% (-3.6% - 2.7%)
Vienna, Austria	11	-8.3% (-10.8% -	8.0% (6.4% -	5.6% (4.2% -	3.9% (2.8% -	-4.5% (-5.6% -	-11.1% (-12.2%

		-5.8%)	9.6%)	6.9%)	5.0%)	3.4%)	--10.0%)
Vilnius, Lithuania	2	6.8% (1.8% - 11.7%)	1.2% (-2.4% - 4.8%)	-3.9% (-6.9% - -0.4%)	-2.7% (-5.0% - -0.3%)	-5.5% (-8.1% - -2.8%)	-20.3% (-22.9% - -17.7%)
Warsaw, Poland	7	3.3% (-0.2% - 6.8%)	8.9% (6.5% - 11.4%)	1.7% (-0.3% - 3.7%)	-2.5% (-4.1% - -0.8%)	-13.9% (-15.5% - -12.4%)	-21.3% (-22.8% - -19.8%)
Zagreb, Croatia	2	-12.3% (-22.6% - -2.0%)	17.3% (11.1% - 23.5%)	17.8% (13.3% - 22.3%)	15.3% (11.4% - 19.1%)	7.6% (3.9% - 11.4%)	-7.6% (-11.3% - -3.8%)
Zurich, Switzerland	8	-12.6% (-16.7% - -8.6%)	2.8% (0.5% - 5.1%)	7.3% (5.1% - 9.6%)	12.4% (10.6% - 14.2%)	-1.2% (-2.8% - 0.5%)	-6.9% (-8.6% - -5.2%)

Table A8: Monthly changes in O₃ concentrations relative to the bias-corrected model predictions for cities in North and South America. Values in *italic* denote values that are statistically different from business-as-usual (p<0.001 based on Kolmogorov-Smirnov test).

Location	#	Jan-20	Feb-20	Mar-20	Apr-20	May-20	Jun-20
Atlanta, USA	1	N/A	7.4% (-8.5% - 23.2%)	-3.4% (-8.1% - 1.3%)	-0.9% (-4.7% - 3.0%)	-3.9% (-8.1% - 0.3%)	-9.9% (-14.5% - -5.3%)
Boston, USA	3	6.1% (2.9% - 9.4%)	8.4% (5.4% - 11.3%)	6.2% (4.0% - 8.3%)	1.9% (-0.2% - 4.1%)	-4.5% (-6.6% - -2.1%)	-7.9% (-10.1% - -5.6%)
Denver, USA	4	7.3% (4.1% - 10.6%)	13.5% (10.3% - 16.7%)	-1.0% (-3.4% - 1.5%)	7.6% (5.3% - 9.9%)	6.1% (4.1% - 8.1%)	-0.6% (-2.4% - 1.3%)
Edmonton, Canada	3	0.5% (-4.0% - 5.0%)	1.0% (-2.4% - 4.3%)	-2.9% (-5.2% - 0.2%)	3.1% (1.2% - 5.1%)	-7.7% (-9.6% - -5.4%)	-5.3% (-7.8% - -2.6%)
Honolulu, USA	1	1.0% (-2.3% - 4.4%)	-6.7% (-9.7% - -3.2%)	-9.2% (-12.4% - -5.6%)	-6.4% (-10.5% - -2.3%)	-18.0% (-22.0% - -14.1%)	-15.9% (-20.6% - -11.2%)
Los Angeles, USA	7	1.0% (-1.9% - 3.9%)	10.0% (7.5% - 12.4%)	-2.5% (-4.5% - 0.6%)	-4.9% (-6.6% - -3.2%)	-5.7% (-7.3% - -4.1%)	-3.6% (-5.2% - -2.0%)
Medellin, Colombia	5	1.3% (-3.6% - 6.3%)	-4.2% (-8.1% - 0.2%)	19.0% (15.0% - 23.0%)	26.0% (21.0% - 31.0%)	8.5% (3.1% - 13.9%)	-14.8% (-20.2% - -9.4%)
Miami, USA	2	3.2% (-3.7% - 10.4%)	-5.8% (-10.9% - -0.8%)	1.2% (-2.0% - 4.4%)	-8.2% (-12.7% - -4.1%)	N/A	N/A
Montreal, Canada	8	5.0% (2.5% - 7.5%)	6.0% (3.8% - 8.1%)	3.1% (1.4% - 4.7%)	3.6% (2.0% - 5.2%)	-2.8% (-4.3% - -1.3%)	-9.2% (-10.8% - -7.6%)
New York, USA	7	6.5% (2.9% - 10.1%)	18.5% (14.9% - 22.1%)	15.1% (12.8% - 17.4%)	15.3% (13.4% - 17.3%)	6.7% (4.7% - 8.7%)	-4.4% (-6.3% - -2.5%)
Oklahoma City, USA	3	7.6% (3.1% - 12.0%)	9.1% (6.1% - 12.2%)	-4.0% (-6.5% - -1.4%)	-3.8% (-5.7% - -1.8%)	1.8% (-0.6% - 3.8%)	6.0% (4.0% - 8.1%)
Phoenix, USA	14	-2.5% (-4.8% - -0.3%)	3.7% (2.0% - 5.3%)	3.0% (1.6% - 4.4%)	4.6% (3.5% - 5.8%)	0.3% (-0.7% - 1.3%)	-2.0% (-3.0% - -1.0%)
Quito, Ecuador	8	-9.8% (-13.2% - -6.5%)	-7.1% (-10.1% - -4.0%)	6.3% (3.4% - 9.1%)	37.4% (33.7% - 41.1%)	11.7% (8.1% - 15.2%)	5.9% (2.4% - 9.4%)
Rio de Janeiro, Brazil	6	-7.2% (-11.3% - -3.2%)	-5.7% (-9.8% - -1.6%)	4.0% (-0.1% - 8.1%)	23.9% (19.6% - 28.2%)	17.6% (13.5% - 21.8%)	11.3% (7.0% - 15.7%)
Salt Lake City, USA	3	29.6% (22.6% - 36.6%)	12.3% (7.5% - 17.2%)	-1.4% (-4.4% - 1.5%)	1.1% (-1.6% - 3.7%)	3.1% (0.8% - 5.5%)	-2.0% (-4.2% - 0.3%)
San Francisco, USA	6	-0.9% (-3.5% - 1.8%)	8.5% (5.9% - 11.0%)	7.1% (5.3% - 8.9%)	-2.2% (-3.9% - -0.5%)	3.6% (1.8% - 5.5%)	-3.4% (-5.6% - -1.3%)
Santiago de Chile, Chile	3	-2.0% (-5.8% - 1.7%)	-14.5% (-18.6% - -10.6%)	-6.9% (-11.0% - -2.7%)	12.3% (7.1% - 17.4%)	6.7% (0.3% - 13.1%)	3.1% (-7.2% - 13.4%)
Seattle, USA	1	8.0% (2.2% - 13.8%)	-8.3% (-14.2% - -2.5%)	4.9% (-0.2% - 9.9%)	6.7% (1.9% - 11.5%)	5.2% (0.7% - 9.7%)	-3.4% (-9.0% - 2.1%)
St. Louis, USA	3	-5.3% (-12.7% - 2.1%)	9.5% (5.4% - 13.6%)	-13.9% (-16.9% - -10.9%)	-7.3% (-9.9% - -4.7%)	-6.6% (-9.4% - -4.0%)	-3.5% (-5.8% - -0.8%)
Washington DC, USA	8	8.5% (5.2% - 11.9%)	11.1% (8.7% - 13.5%)	-2.2% (-3.8% - 0.6%)	0.2% (-1.3% - 1.7%)	-3.6% (-5.1% - -2.1%)	-1.3% (-2.8% - 0.2%)

625 *Data availability.* The model output and air quality observations used in this study are all publicly available (see methods). The output from the GEOS-CF sensitivity simulation as well as the bias-corrected model predictions are available from CAK per request.

630 *Author contributions.* CAK and MJE designed the study and conducted the main analyses. CAH and SM contributed OpenAQ observations. TO provided observations and interpretations for Japan. FCM and BBF provided observations and interpretations for Rio de Janeiro, and MVDS provided observations and interpretations for Quito. RGR provided observations for Melbourne and helped analyze results for Australia. KEK and RAL conducted the GEOS-CF simulations. KEK and CAK conducted the GEOS-CF sensitivity experiments and forecasts. LHF conducted NO_x to NO₂ sensitivity simulations. SP contributed to overall study design and context discussion. All authors contributed to the writing.

Competing interests. The authors declare that they have no conflict of interest.

640 *Acknowledgements.* Resources supporting the model simulations were provided by the NASA Center for Climate Simulation at the Goddard Space Flight Center (<https://www.nccs.nasa.gov/services/discover>). We thank Jenny Fisher (U. Wollongong, Australia) for helpful discussions. CAK, KEK and SP acknowledge support by the NASA Modeling, Analysis and Prediction (MAP) Program. MJE and LHF are thankful for support from the University of York's Viking, HPC facility.

References

Boersma, K.F., H.J. Eskes, R. J. Dirksen, R. J. van der A, J. P. Veefkind, P. Stammes, V. Huijnen, Q. L. Kleipool, M. Sneep, J. Claas, J. Leitao, A. Richter, Y. Zhou, and D. Brunner. An improved retrieval of tropospheric NO₂ columns from the Ozone Monitoring Instrument, *Atmos. Meas. Tech.* 4, 1905-1928, doi:10.5194/amt-4-1905-2011, 2011.

Castellanos, P., and F. Boersma. Reductions in nitrogen oxides over Europe driven by environmental policy and economic recession, *Sci. Rep.*, 265, doi:10.1038/srep00265, 2012.

Chen, T. and C. Guestrin. XGBoost: A Scalable Tree Boosting System, *CoRR*, abs/1603.02754, 785–794, <https://doi.org/10.1145/2939672.2939785>, 2016.

655 Crippa, M., Solazzo, E., Huang, G. et al. High resolution temporal profiles in the Emissions Database for Global Atmospheric Research. *Sci Data* 7, 121 (2020). <https://doi.org/10.1038/s41597-020-0462-2>, 2020.

660 Crippa, M., Guizzardi, D., Muntean, M., Schaaf, E., Dentener, F., van Aardenne, J. A., Monni, S., Doering, U., Olivier, J. G. J., Pagliari, V., and G. Janssens-Maenhout. Gridded emissions of air pollutants for the period 1970–2012 within EDGAR v4.3.2, *Earth Syst. Sci. Data*, 10, 1987–2013, <https://doi.org/10.5194/essd-10-1987-2018>, 2018.

- Dantas, G., Siciliano, B., França, B.B., da Silva, C.M., and G. Arbilla. The impact of COVID-19 partial lockdown on the air quality of the city of Rio de Janeiro, Brazil, *Science of The Total Environment*, Volume 729, <https://doi.org/10.1016/j.scitotenv.2020.139085>, 2020.
- 665 Darmenov, A.S., and A. da Silva. The Quick Fire Emissions Dataset (QFED)—Documentation of versions 2.1, 2.2 and 2.4. Technical Report Series on Global Modeling and Data Assimilation. NASA/TM-2015-104606, Vol. 38, 212 pp., 2015.
- Djalalova, I., Delle Monache, L., and J. Wilczak. PM2.5 analog forecast and Kalman filter post-processing for the Community Multiscale Air Quality (CMAQ) model, *Atmospheric Environment*,
670 Volume 108, Pages 76-87, <https://doi.org/10.1016/j.atmosenv.2015.02.021>, 2015.
- Duncan, B. N., L. N. Lamsal, A. M. Thompson, Y. Yoshida, Z. Lu, D. G. Streets, M. M. Hurwitz, and K. E. Pickering. A space-based, high-resolution view of notable changes in urban NO_x pollution around the world (2005–2014). *J. Geophys. Res.* 121, 976–996, 2016.
- Eslami, E., Salman, A.K., Choi, Y., Sayeed, A. and Y. Lops. A data ensemble approach for real time air
675 quality forecasting using extremely randomized trees and deep neural networks, 518 *Neural Comput. Appl.*, 1-17, 2019.
- Frery, J., Habrard, A., Sebban, M., Caelen, O., and L. He-Guelton. Efficient Top Rank Optimization with Gradient Boosting for Supervised Anomaly Detection, *Machine Learning and Knowledge
Discovery in Databases, Ecml Pkdd 2017, Pt I*, 10534, 20–35, [https://doi.org/10.1007/978-3-319-71249-
680 9_2](https://doi.org/10.1007/978-3-319-71249-9_2), 2017.
- Friedman, J. H.: Greedy function approximation: A gradient boosting machine., *The Annals of Statistics*, 29, 1189–1232, <https://doi.org/10.1214/aos/1013203451>,
<http://projecteuclid.org/euclid.aos/1013203451>, 2001.
- Grange, S. K. and D. C. Carslaw. Using meteorological normalisation to detect interventions in air
685 quality time series, *Science of The Total Environment*, 653, 578–588,
<https://doi.org/10.1016/j.scitotenv.2018.10.344>, [https://linkinghub.elsevier.com/retrieve/pii/
S004896971834244X](https://linkinghub.elsevier.com/retrieve/pii/S004896971834244X), 2019.
- Grange, S. K., Carslaw, D. C., Lewis, A. C., Boleti, E., and C. Hueglin. Random forest meteorological
normalisation models for Swiss PM 10 trend analysis, *Atmospheric Chemistry and Physics*, 18, 6223–
690 6239, <https://doi.org/10.5194/acp-18-6223-2018>, <https://www.atmos-chem-phys.net/18/6223/2018/>,
2018.
- Hilboll, A., A. Richter, and J. P. Burrows. Long-term changes of tropospheric NO₂ over megacities
derived from multiple satellite instruments, *Atmos. Chem. Phys.*, 13, 4145–4169, doi:10.5194/acp-13-
4145-2013, 2013.
- 695 Hu, L., Keller, C. A., Long, M. S., Sherwen, T., Auer, B., Da Silva, A., Nielsen, J. E., Pawson, S.,
Thompson, M. A., Trayanov, A. L., Travis, K. R., Grange, S. K., Evans, M. J., and D. J. Jacob. Global

simulation of tropospheric chemistry at 12.5 km resolution: performance and evaluation of the GEOS-Chem chemical module (v10-1) within the NASA GEOS Earth system model (GEOS-5 ESM), *Geosci. Model Dev.*, 11, 4603–4620, <https://doi.org/10.5194/gmd-11-4603-2018>, 2018.

700 Ivatt, P. D. and M. J. Evans. Improving the prediction of an atmospheric chemistry transport model using gradient boosted regression trees, *Atmos. Chem. Phys. Discuss.*, <https://doi.org/10.5194/acp-2019-753>, in review, 2019.

Janssens-Maenhout, G., Crippa, M., Guizzardi, D., Dentener, F., Muntean, M., Pouliot, G., Keating, T., Zhang, Q., Kurokawa, J., Wankmüller, R., Denier van der Gon, H., Kuenen, J. J. P., Klimont, Z., Frost, 705 G., Darras, S., Koffi, B., and Li, M.: HTAP_v2.2: a mosaic of regional and global emission grid maps for 2008 and 2010 to study hemispheric transport of air pollution, *Atmos. Chem. Phys.*, 15, 11411–11432, <https://doi.org/10.5194/acp-15-11411-2015>, 2015.

Jhun I, Coull BA, Zanobetti A, P. Koutrakis. The impact of nitrogen oxides concentration decreases on ozone trends in the USA. *Air Qual Atmos Health*. 2015;8(3):283-292. doi:10.1007/s11869-014-0279-2, 710 2015.

Kang, D., C. Hogrefe, K. Foley, S. Napelenok, R. Mathur, and S. T. Rao. Application of the Kolmogorov-zurbenko filter and the decoupled direct 3D method for the dynamic evaluation of a regional air quality model, *Atmos. Environ.*, 80, 58-69, 2013.

Keller, C. A., Long, M. S., Yantosca, R. M., Da Silva, A. M., Pawson, S., and D. J. Jacob. HEMCO 715 v1.0: a versatile, ESMF-compliant component for calculating emissions in atmospheric models, *Geosci. Model Dev.*, 7, 1409–1417, <https://doi.org/10.5194/gmd-7-1409-2014>, 2014.

Keller, C.A., Knowland, K.E., Duncan, B.N., Liu, J., Anderson, D.C., Das, S., Lucchesi, R.A., Lundgren, E.W., Nicely, J.M., Nielsen, J.E., et al. Description of the NASA GEOS Composition Forecast Modeling System GEOS-CF v1.0, *Earth and Space Science Open Archive*, 38, 720 <https://doi.org/10.1002/essoar.10505287.1>, 2020.

Kleinert, F., Leufen, L. H., and Schultz, M. G.: IntelliO3-ts v1.0: A neural network approach to predict near-surface ozone concentrations in Germany, *Geosci. Model Dev. Discuss.*, <https://doi.org/10.5194/gmd-2020-169>, in review, 2020.

Knowland, K.E., C.A. Keller, and R. Lucchesi, File Specification for GEOS-CF Products. GMAO 725 Office Note No. 17 (Version 1.1), 37 pp, available from http://gmao.gsfc.nasa.gov/pubs/office_notes, 2020.

Lamsal, L. N., Martin, R. V., Padmanabhan, A., van Donkelaar, A., Zhang, Q., Sioris, C. E., Chance, K., Kurosu, T. P., and M. J. Newchurch. Application of satellite observations for timely updates to global anthropogenic NO_x emission inventories, *Geophys. Res. Lett.*, 38, L05810, 730 doi:[10.1029/2010GL046476](https://doi.org/10.1029/2010GL046476), 2011.

- Lamsal, L. N., R. V. Martin, D. D. Parrish, and N. A. Krotkov. Scaling relationship for NO₂ pollution and urban population size: A satellite perspective, *Environ. Sci. Technol.*, 47(14), 7855–7861, doi:10.1021/es400744g, 2013.
- 735 Le, T., Wang, Y., Liu, L., Yang, J., Yung, Y.L., Li, G., and J.H. Seinfeld. Unexpected air pollution with marked emission reductions during the COVID-19 outbreak in China, *Science*, doi:10.1126/science.abb7431, 2020.
- Le Quéré, C., Jackson, R.B., Jones, M.W. et al. Temporary reduction in daily global CO₂ emissions during the COVID-19 forced confinement. *Nat. Clim. Chang.*, <https://doi.org/10.1038/s41558-020-0797-x>, 2020.
- 740 Liu F., et al. Abrupt decline in tropospheric nitrogen dioxide over China after the outbreak of COVID-19, *Science Advances*, DOI: 10.1126/sciadv.abc2992, 2020a.
- Liu, Z. et al. COVID-19 causes record decline in global CO₂ emissions. <http://arxiv.org/abs/2004.13614>, 2020b.
- 745 Long, M. S., Yantosca, R., Nielsen, J. E., Keller, C. A., da Silva, A., Sulprizio, M. P., Pawson, S., and D.J. Jacob. Development of a grid-independent GEOS-Chem chemical transport model (v9-02) as an atmospheric chemistry module for Earth system models, *Geosci. Model Dev.*, 8, 595–602, <https://doi.org/10.5194/gmd-8-595-2015>, 2015.
- Lucchesi, R., File Specification for GEOS-5 FP-IT. GMAO Office Note No. 2 (Version 1.4) 58 pp, available from http://gmao.gsfc.nasa.gov/pubs/office_notes.php, 2015.
- 750 Lundberg, S. M. & Lee, S.-I. A unified approach to interpreting model predictions. *Adv. Neural Inf. Process. Syst.* 30, 4768–4777, 2017.
- Lundberg, S.M., Erion, G., Chen, H. et al. From local explanations to global understanding with explainable AI for trees. *Nat Mach Intell* 2, 56–67, <https://doi.org/10.1038/s42256-019-0138-9>, 2020.
- 755 Ministry of the Environment (MOE), Government of Japan. The Atmospheric Environmental Regional Observation System (AEROS), data available at <http://soramame.taiki.go.jp/Index.php> (last access: July 3, 2020), 2020. (in Japanese)
- 760 Pagowski, M., Grell, G.A., Devenyi, D., Peckham, S.E., McKeen, S.A., Gong, W., Delle Monache, L., McHenry, J.N., McQueen, J., and P. Lee. Application of dynamic linear regression to improve the skill of ensemble-based deterministic ozone forecasts, *Atmospheric Environment*, Volume 40, Issue 18, 3240-3250, <https://doi.org/10.1016/j.atmosenv.2006.02.006>, 2006.
- Petetin, H., Bowdalo, D., Soret, A., Guevara, M., Jorba, O., Serradell, K., and Pérez García-Pando, C.: Meteorology-normalized impact of the COVID-19 lockdown upon NO₂ pollution in Spain, *Atmos. Chem. Phys.*, 20, 11119–11141, <https://doi.org/10.5194/acp-20-11119-2020>, 2020.

- Russell, A. R., L. C. Valin, and R. C. Cohen. Trends in OMI NO₂ observations over the United States: Effects of emission control technology and the economic recession, *Atmos. Chem. Phys.*, 12(24), 12,197–12,209, 2012.
- 765 Shah, V., Jacob, D. J., Li, K., Silvern, R. F., Zhai, S., Liu, M., Lin, J., and Zhang, Q. (2020). Effect of changing NO_x lifetime on the seasonality and long-term trends of satellite-observed tropospheric NO₂ columns over China, *Atmos. Chem. Phys.*, 20, 1483–1495, <https://doi.org/10.5194/acp-20-1483-2020>.
- 770 2020.
- Seinfeld, J.H. and S.N. Pandis. *Atmospheric Chemistry and Physics: From Air Pollution to Climate Change*. John Wiley & Sons, Hoboken, 2016.
- Streets, D.G., Canty T., Carmichael, G.R. , de Foy, B. Dickerson, R.R, Duncan, B.N., Edwards, D.P. , Haynes, J.A., Henze, D.K., Houyoux, M.R., Jacob, D.J., Krotkov, N.A., Lamsal, L.N., Liu, Y., Lu, Z., Martin, R.V., Pfister, G.G., Pinder, R.W., Salawitch, R.J., and K.J. Wecht, Emissions estimation from satellite retrievals: A review of current capability, *Atmospheric Environment*, Volume 77, Pages 1011-1042, <https://doi.org/10.1016/j.atmosenv.2013.05.051>, 2013.
- 775
- Tobías, A., Carnerero, C., Reche, C., Massagué, J., Via, M., Minguillón, M. C., Alastuey, A., and X. Querol. Changes in air quality during the lockdown in Barcelona (Spain) one month into the SARS-CoV-2 epidemic, *Science of The Total Environment*, 726, 138 540, 540 <https://doi.org/10.1016/j.scitotenv.2020.138540>, 2020.
- 780
- Wargan, K., Pawson, S., Olsen, M.A., Witte, J.C., Douglass, A.R., Ziemke, J.R., Strahan, S.E., and J. E. Nielsen. The Global Structure of Upper Troposphere-Lower Stratosphere Ozone in GEOS-5: A Multi-Year Assimilation of EOS Aura Data. *J. Geophys. Res. - Atmos*, 120, 2013-2036. doi: 10.1002/2014JD022493, 2015.
- 785